Research Square

Preprints are preliminary reports that have not undergone peer review.
They should not be considered conclusive, used to inform clinical practice,
or referenced by the media as validated information.

Native-to-fibril structural remodelling reveals an amyloid-selective transthyretin epitope for AI-guided binder design

Ugo Lomoio
Magna Graecia University
Valentina Carbonari
Magna Graecia University
Paola Roncada
Magna Graecia University
Andrea Urbani
Università Cattolica del Sacro Cuore
Pietro Lio'
University of Cambridge
Pierangelo Veltri
University of Calabria
Pietro Hiram Guzzi
hguzzi@unicz.it

Magna Graecia University

Article

Keywords:

Posted Date: November 3rd, 2026

DOI: https://doi.org/10.21203/rs.3.rs-11583001/v1

License: This work is licensed under a Creative Commons Attribution 4.0 International License.
Read Full License

Additional Declarations: No competing interests reported.

Native-to-fibril structural remodelling reveals an amyloid-selective transthyretin epitope for AI-guided binder design

Ugo Lomoio[1], Valentina Carbonari[1], Paola Roncada[2], Andrea Urbani[3,4], Pietro Lió[5], Pierangelo Veltri[6], and Pietro Hiram Guzzi[1]

[1]Department of Surgical and Medical Sciences, University of Catanzaro, Catanzaro, Italy
[2]Department of Health Sciences, University of Catanzaro, Catanzaro, Italy
[3]Fondazione Policlinico Universitario Gemelli
[4]Catholic University of the Sacred Heart, Roma, Italy
[5]Department of Computer Science and Technology, Cambridge University, Cambridge, United Kingdom
[6]Department of Computer Science Modelling and Systems, University of Calabria, Rende, Italy

Abstract

Transthyretin (TTR) amyloidosis involves conversion of the native tetramer into cross-β fibrils, creating potential targets for conformation-selective binders. Full-assembly solvent-accessibility analysis of 30 patient-derived fibril structures, spanning wild-type TTR and ten hereditary variants, identifies increased exposure of an N-terminal region adjacent to Cys10. Using a common normalisation reference, mean relative solvent accessibility for residues 11–15 is 0.089 in native TTR and at least 0.168 in fibrils. Modification mapping, saturation-mutagenesis stability predictions and steric PTM models provide molecular context. BoltzGen and RFAntibody generate candidate binders, and sequence-only Boltz-2 counter-predictions place selected nanobodies at the Pro11/Met13/Lys15 region in fibril-derived constructs but at distal surfaces in native-state constructs. Vitreous-fibril designs also engage cardiac-fibril constructs, suggesting cross-tissue epitope recognition. These results support structure-guided candidate prioritisation, while fibril geometry, binding affinity and disease-state selectivity require experimental validation.

1 Introduction

Transthyretin (TTR) is a homotetrameric plasma protein synthesised primarily in the liver and choroid plexus. It transports thyroxine (T4) and retinol [1, 2, 3]. Its four identical subunits, each approximately 14 kDa, form a stable, β-sheet-rich tetramer. Genetic mutations, post-translational modifications (PTMs) and proteolytic cleavage can destabilise this assembly, facilitating dissociation into monomers that misfold and aggregate into insoluble amyloid fibrils [4, 5]. This process underlies hereditary transthyretin amyloidosis (ATTRv) and wild-type transthyretin amyloidosis (ATTRwt), which affect the peripheral nerves, heart and other organs [6, 7].

More than 150 pathogenic TTR variants have been reported, with Val30Met the most prevalent in endemic populations [4, 8]. Computational studies have systematically characterised the structural and functional consequences of these mutations [9]. The contribution of PTMs to TTR immunogenicity and disease progression has received less attention, although Cys10 modifications (S-sulphonation, S-cysteinylation and S-glutathionylation), age-related oxidation, isoaspartate formation and proteolytic cleavage can modulate TTR stability and amyloidogenicity [10, 11, 12].

PTMs encompass chemical alterations, including oxidation, deamidation, glycation, phosphorylation, ubiquitination and proteolytic cleavage, that influence protein folding, stability, interactions and degradation [13]. The PTM landscape changes with age as oxidative damage increases, enzymatic activity changes and metabolic stress accumulates [14, 15]. Declining proteostasis can compound these effects through impaired chaperone function and proteasomal degradation, allowing aberrantly modified proteins to accumulate [16, 17]. In TTR, oxidative modifications at methionine 30 and cysteine 10 have been reported to impair tetramer stability and enhance fibrillogenesis in vitro [18]. Modified species have also been identified in extracted amyloid deposits [19], and PTM patterns change with advancing age [20, 21].

Interactions between genetic variation and age-associated PTMs may therefore link declining proteostasis to TTR amyloidogenesis [22, 23].

Cys10 PTMs can also affect TTR's physiological transport function. S-glutathionylation, S-cysteinylglycination and S-sulphonation introduce steric bulk near the thyroxine-binding channel and can alter thyroid-hormone binding in a modification-dependent manner; S-glutathionylation has been reported to exert the strongest effect on T3 binding [24, 25, 26]. Redox status and ageing may consequently influence hormone transport and the action of kinetic stabilisers that occupy the same channel.

Ubiquitination and SUMOylation provide additional links between TTR modification and proteostasis. TTR undergoes degradation through the ubiquitin–proteasome system, and declining proteasomal capacity with age may favour the accumulation of ubiquitinated species [10, 27]. SUMOylation at Lys126 has been reported experimentally [28], and TTR can modulate global SUMOylation through interaction with the SUMO-conjugating enzyme Ubc9 [29]. Tyrosine nitration and protein carbonylation further diversify the modified TTR pool under inflammatory and oxidative conditions [10, 25].

ATTR can therefore be viewed as a heterogeneous molecular system in which genetic variation, PTMs, proteolytic processing, conformational transitions and intermolecular interactions jointly shape the proteoform landscape. The present study catalogues 133 TTR point mutations and 26 modified residues across 11 PTM categories, and examines structural features that emerge during the native-to-fibril transition. This heterogeneity also extends beyond individual proteoforms. Amyloid deposits contain associated proteins, extracellular-matrix components, molecular chaperones and lipids that may influence fibril nucleation, propagation, stability, tissue distribution and epitope accessibility. Structural proteomics offers a way to connect proteoform characterisation with the higher-order organisation of these deposits, integrating sequence variation, modification state, conformation and molecular interactions.

ATTRwt also shows marked age and sex differences. Wild-type TTR amyloid cardiomyopathy predominantly affects men, with women accounting for approximately 16% of diagnosed cases [30, 31]. Disease onset usually occurs after age 60, and phenotype and prognosis in women are strongly associated with age at diagnosis [30]. The THAOS registry indicates that the proportion of women increases with age, although presentation remains delayed [32]. These patterns motivate investigation of age- and sex-associated mechanisms of proteostasis, but do not by themselves establish a role for modified TTR species.

Modification- and conformation-specific antibodies offer a potential therapeutic approach. The human antibody NI301A selectively recognises TTR amyloid deposits and promotes phagocytic clearance [33]. Amyloid-depleting candidates include ALXN2220 (NI006), developed from NI301A [33], and coramitug (PRX004), derived from conformation-specific antibodies against amyloidogenic TTR [34]. Antibodies directed against isoaspartate-modified TTR have also shown affinity and selectivity for modified species [35], while other conformation-specific antibodies recognise amyloidogenic TTR forms [34, 36]. These studies support the tractability of modification- and conformation-dependent epitopes and motivate systematic, structure-guided identification of candidate binding sites.

The molecular framework described by Merlini and Bellotti [37] places protein misfolding and pathogenic conformations at the centre of amyloidosis and emphasises molecular diagnosis as a basis for treatment. Subsequent work has further linked molecular understanding with therapeutic development [38, 39]. A broader proteomic companion-diagnostic strategy could extend amyloid typing to molecular phenotyping, characterising the precursor proteoform, PTM pattern, proteolytic fragments and associated proteins within a deposit. Connecting these features to structural organisation could help prioritise targets for therapy. In parallel, advances in AI-guided protein design provide tools for generating candidate binders. BoltzGen uses diffusion-based generative models to design nanobodies and antibodies against specified target sites [40]. RFAntibody combines RFdiffusion for backbone generation [41], ProteinMPNN for sequence assignment [42] and RoseTTAFold2 for structural assessment. Boltz-2 predicts antibody–target complexes and provides confidence scores for ranking [43]. Together with patient-derived cryo-EM fibril structures [44, 45, 46], these methods support computational exploration of amyloid-selective binder design.

The present study maps solvent accessibility across 30 patient-derived TTR fibril structures available at the data-retrieval date, spanning wild-type TTR and ten hereditary variants from cardiac, vitreous and skeletal-muscle deposits. Comparison with the native tetramer identifies an N-terminal candidate epitope centred on Pro11, Met13 and Lys15, adjacent to the Cys10 modification hotspot. This region is relatively buried in native TTR and more exposed across the fibril panel. Solvent-exposure mapping has informed individual fibril-structure studies [47]; the analysis here integrates the deposited panel with a native-state reference and uses the resulting accessibility map to guide binder design. Saturation-mutagenesis stability predictions for all 2,413 single mutants, steric models of three oxidative Cys10 modifications and T-cell

epitope predictions overlapping modification sites provide complementary molecular context.

Generative binder design extends approaches previously applied to other amyloid systems, including de novo fibril-capping inhibitors of tau, Aβ and α-synuclein [48], and binders recognising amyloidogenic segments [49]. Here, BoltzGen and RFAntibody were used in design campaigns against a native-state surrogate, the 6SDZ fibril and the F64S vitreous-fibril structure. Selected leads were then assessed by Boltz-2 counter-prediction against fibril-derived and native-state constructs. The predicted interfaces include the intended N-terminal epitope in fibril-derived constructs, whereas alternative surfaces are contacted in native-state constructs. These results prioritise candidates for experimental testing; they do not establish selective binding to experimental fibrils or exclude binding to native TTR.

The computational pipeline comprises five components: (1) a catalogue of 26 unique modified residues (27 site/modification pairs, with Lys126 assigned both ubiquitination and SUMOylation) across 11 categories, alongside 133 point mutations; (2) ThermoMPNN saturation-mutagenesis $\Delta\Delta G$ predictions for all 2,413 single mutants [50]; (3) Boltz-2 steric approximations of three oxidative Cys10 modifications [43]; (4) full-assembly solvent-accessibility comparisons between native TTR and cryo-EM fibril structures; and (5) candidate-binder design and ranking using BoltzGen [40], RFAntibody and Boltz-2 interface-confidence analysis. The AlphaFold3 structures are reused from the earlier mutational-landscape study [9]; the present work instead focuses on conformational differences between native and fibrillar TTR and their implications for target-site selection.

Structural proteomics could provide a future experimental link between patient-specific molecular phenotyping and this computational workflow. Measurements of protein accessibility, limited proteolysis, chemical or cross-linking footprints, intermolecular interactions and conformational protection could supply structural restraints without requiring atomic-resolution analysis of every patient-derived assembly. Integration with cryo-EM structures and AI-based modelling could help distinguish conserved TTR amyloid surfaces from variant-, PTM-, interactome- or tissue-dependent features. Such measurements would also test whether predicted epitopes remain accessible within the molecular environment of an individual deposit. Patient-derived restraints could subsequently inform binder design and counter-prediction, linking proteomic diagnosis, structural phenotyping, target identification and antibody engineering. This proposed extension would require experimental validation of affinity, selectivity and tissue recognition before clinical translation. Figure 1 summarises the current workflow and its potential applications.

2 Results

2.1 Expanded PTM and modification catalogue

The compiled catalogue comprises 159 entries: 133 point mutations (87 pathogenic, 9 likely pathogenic, 9 variants of uncertain significance, 1 benign, 1 likely benign, 25 not found and 1 unknown) and 26 unique modified residues (27 site/modification pairs, with Lys126 assigned both ubiquitination and SUMOylation) across 11 categories (Table 1). The PTM catalogue includes established Cys10 thiol modifications (S-sulphonation, S-cysteinylation, S-glutathionylation and S-glycinylcysteinylation), oxidation (Cys10 sulfonic acid and Met13 sulfoxide), isoaspartate formation (Asp99), proteolytic cleavage (positions 49 and 58), N-linked glycosylation (Asn98), phosphorylation (Ser52) and 4-carboxyglutamate formation (Glu42). Four additional categories comprise ubiquitination (8 lysine sites: K9, K15, K35, K48, K70, K76, K80 and K126), SUMOylation (Lys126, reported experimentally [28]), tyrosine nitration (5 sites: Y69, Y78, Y105, Y114 and Y116) and non-site-specific carbonylation of K/R/P/T residues. Three RNA isoforms (canonical TTR-201, truncated TTR-204 and deleted TTR-212) and 7 predicted m6A consensus motifs were also identified. No TTR-specific A-to-I RNA-editing sites were identified in REDIportal.

2.2 Saturation mutagenesis reveals a broad stability landscape

ThermoMPNN, a graph neural network trained on the MegaScale dataset [50], was used to predict the stability effects of all amino-acid substitutions in the 127-residue TTR monomer. Site-saturation analysis yielded $\Delta\Delta G$ predictions for 2,413 unique single mutants. The predicted landscape is biased towards destabilisation: mean $\Delta\Delta G$ was $1.02\,\mathrm{kcal\,mol^{-1}}$ (median $0.74\,\mathrm{kcal\,mol^{-1}}$), with 984 mutations (41%) predicted to destabilise the fold by more than $1\,\mathrm{kcal\,mol^{-1}}$ and 477 by more than $2\,\mathrm{kcal\,mol^{-1}}$ (Fig. 3A). Positions with the largest predicted destabilising effects cluster in the β-sheet core and C-strand region, with glycine and proline substitutions prominent among the most destabilising variants.

The 133 catalogued mutations tend towards the destabilising end of this landscape, with a median $\Delta\Delta G$ of $1.41\,\mathrm{kcal\,mol^{-1}}$ and a median percentile of 68.7 in the saturation distribution (Fig. 3A). The

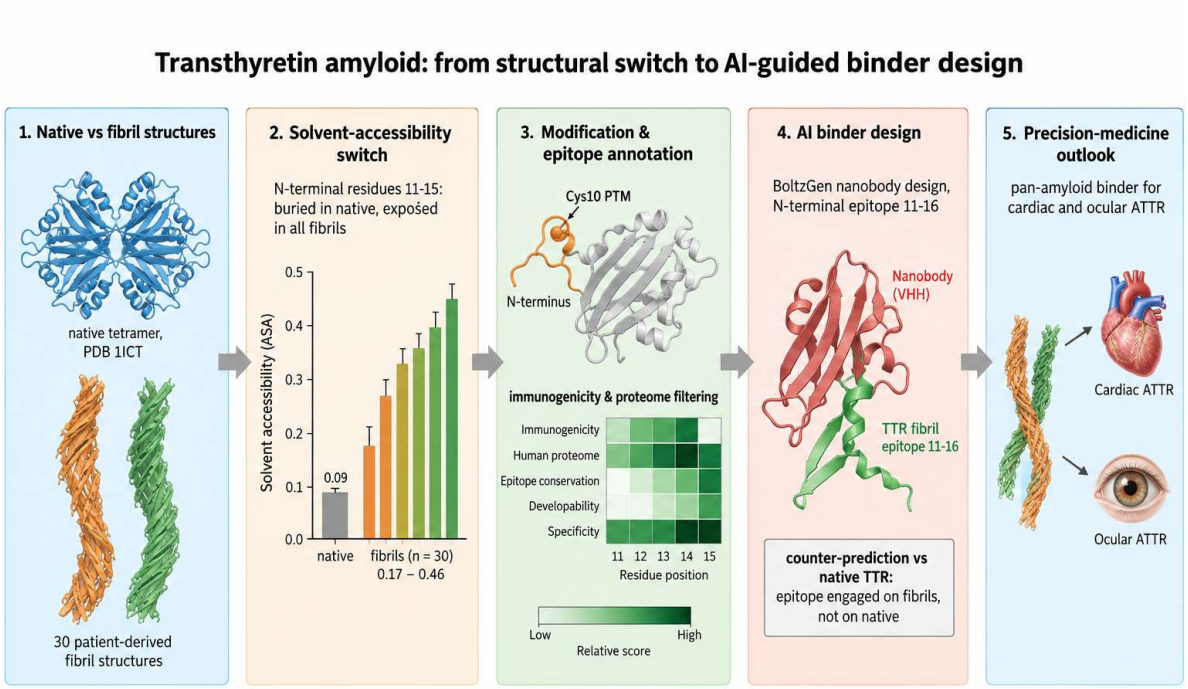


Figure 1: **Workflow overview.** Native and patient-derived fibril structures are compared by full-assembly solvent-accessibility analysis, revealing an N-terminal amyloid-selective exposure switch (residues 11–15). The epitope is annotated against the modification and immunogenicity landscape, targeted by AI-guided nanobody design (BoltzGen) with Boltz-2 counter-prediction against native TTR, and evaluated across cardiac- and vitreous-derived constructs. Potential diagnostic and therapeutic applications remain prospective.

largest predicted destabilising effects include Y69I ($\Delta\Delta G = 3.49\,\mathrm{kcal\,mol^{-1}}$), G67E (3.34), G53E (3.20), R34G (3.00) and V32G (2.97). This sequence-wide profile provides context for the structural analysis. Because the predictions concern monomer stability, they do not directly quantify tetramer dissociation, epitope exposure or immunogenicity.

2.3 Structural impact of the catalogued mutations

AlphaFold3 structures for all 133 mutations were reused from a previous study [9]. TM-scores relative to wild-type TTR indicated high structural conservation (mean 0.965, range 0.938–0.992), consistent with predominantly local changes in the predicted structures (Fig. 4A). Solvent-accessibility analysis classified 67 of 133 mutation sites as surface-exposed (RSA $>$ 0.25), providing an initial indication of potential accessibility for antibody recognition (Fig. 4B,C).

Among the 12 original PTM sites, 3 were surface-exposed in the wild-type structure: Asp99 (isoaspartate, RSA = 0.57), Ser52 (phosphorylation, RSA = 0.42) and Glu42 (4-carboxyglutamate, RSA = 0.48). Other sites, including Cys10 (RSA = 0.19), Asn98 (RSA = 0.08) and Met13 (RSA = 0.23), were relatively buried, motivating direct comparison with their accessibility in the amyloid state.

2.4 Cys10 post-translational modifications: steric accommodation models

Cys10 is the dominant PTM site in circulating TTR (>85% modified [10]) and is associated with the thyroxine-binding-channel region. Three Boltz-2 models examined whether modification-associated steric bulk could be accommodated in the tetramer: (i) cysteine sulfonic acid, representing Cys10 oxidation and chemically distinct from S-sulphonation, which was not modelled; (ii) a glutathione (GSH) molecule near Cys10 as an approximation of S-glutathionylation; and (iii) a cysteinylglycine dipeptide as an approximation of S-cysteinylglycination. These are *steric approximations*: explicit covalent bonds were

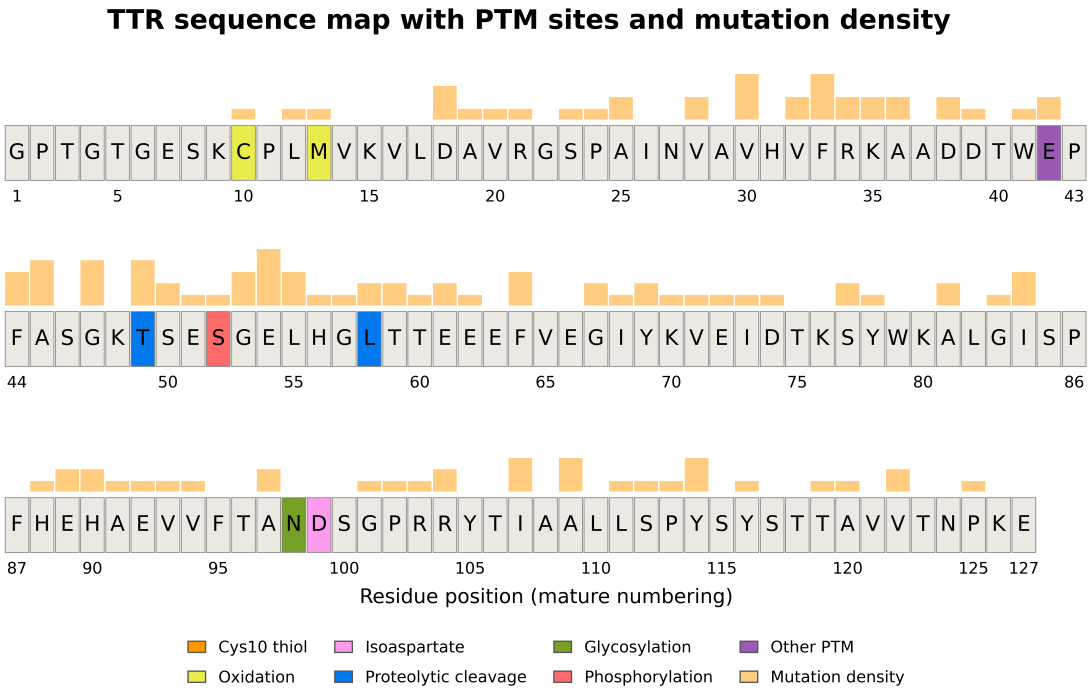


Figure 2: **Modification landscape of human TTR.** Sequence map of the 133 catalogued point mutations and 26 unique modified residues (27 site/modification pairs; Lys126 carries both ubiquitination and SUMOylation) across 11 categories, with mutation density indicated above the sequence.

not specified, so the models represent adduct size and placement rather than covalent geometry. Complex ipTM values were 0.936–0.946, comparable to the wild-type tetramer baseline of 0.942 (Fig. 5B). The predicted placements are compatible with accommodation near the channel without a major global rearrangement, although confidence scores do not establish structural stability. Per-ligand ipTM values relative to the four TTR chains were 0.65–0.81. N-terminal solvent accessibility (residues 1–20) changed little: Cys10 remained relatively buried (RSA = 0.17–0.20, compared with 0.17 in wild-type), as did residues 11–14 (Fig. 5A). Within the limitations of the models, steric accommodation of these moieties therefore did not reproduce the N-terminal exposure observed in the experimental fibril structures.

2.5 Sequence-level immunogenicity and human-proteome filtering provide complementary candidate annotation

Sequence-level epitope predictions provided complementary annotation of the modification landscape. Linear B-cell epitope propensity was estimated from Parker hydrophilicity, Chou–Fasman β-turn propensity and Kolaskar–Tongaonkar antigenicity, using a sequence-specific 60th-percentile threshold. These scores describe propensity, rather than demonstrated immunogenicity. Profiles recomputed for all 133 mutant sequences showed local redistribution of predicted windows, with a mean of 49 non-overlapping windows per sequence, as in wild-type TTR. Of the 133 variants, 44 (33%) generated at least one new window overlapping the mutation site and 39 removed at least one (Fig. 6). F33C generated 7 new windows, I84S generated 5, and I84N and I73V generated 4 each. MHCflurry 2.0 predictions across 38 HLA-I alleles yielded 202,730 predictions and 1,689 binders at $\leq$2% percentile rank; NetMHCIIpan predictions across 11 HLA-DR alleles yielded 21,956 predictions and 508 binders at <5% rank. Mutation-derived candidates were dominated by V32A, G53E, I107F and L111M, while the Y105/Y114 nitration-site regions produced the highest-ranking PTM-site-overlapping candidates (Supplementary Table S2). Because these methods evaluate standard amino-acid sequences, the results concern *peptides overlapping modification sites*, not chemically modified peptides. Screening all 2,255 unique candidate peptides against the reviewed UniProt Swiss-Prot human proteome used length-dependent thresholds: 100% identity for 8–9mers, $\geq$80% for 10–15mers and $\geq$67% for peptides longer than 15 residues. This sequence-similarity filter does not assess cross-reactivity or safety. Eighteen peptides, all MHC-I candidates, were flagged; none of the 43 top-ranked candidates was flagged (Fig. 7). Detailed rankings are provided in the Supplementary Data.

Table 1: Expanded PTM catalogue for human transthyretin. Categories newly included in the catalogue are shown in bold. Entries include both experimental annotations and predictions.

PTM category	Site(s)	Mature pos.	RSA	Exposed	Evidence
Cys10 thiol (4)	Cys10	10	0.187	No	Experimental
Oxidation (2)	Cys10, Met13	10, 13	0.187, 0.225	No	Experimental
Isoaspartate (1)	Asp99	99	0.571	Yes	Predicted
Proteolytic cleavage (2)	pos 49, 58	49, 58	0.008, 0.116	No	Experimental
N-glycosylation (1)	Asn98	98	0.083	No	Experimental
Phosphorylation (1)	Ser52	52	0.421	Yes	Experimental
4-carboxyglutamate (1)	Glu42	42	0.475	Yes	Experimental
Ubiquitination (8)	K9,15,35,48,70,76,80,126	various	various	various	Predicted
SUMOylation (1)	K126	126			Experimental
Tyrosine nitration (5)	Y69,78,105,114,116	various	various	various	Predicted
Carbonylation (1)	K/R/P/T	non-specific			Predicted

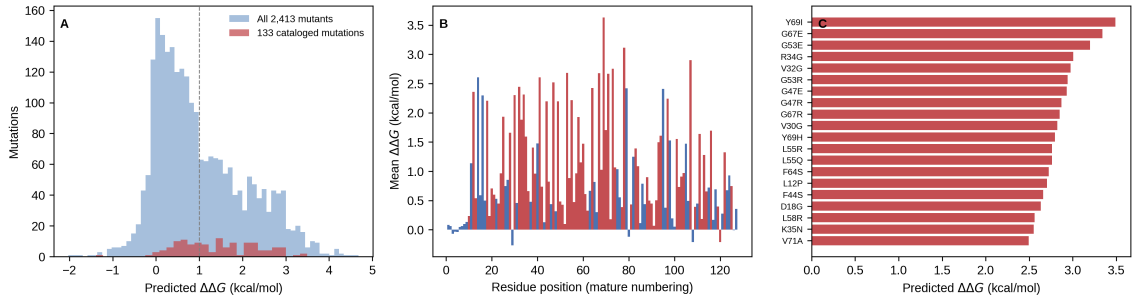


Figure 3: **Saturation-mutagenesis stability landscape of TTR.** (A) Distribution of ThermoMPNN $\Delta\Delta G$ for all 2,413 single mutants, with the 133 catalogued mutations highlighted. (B) $\Delta\Delta G$ per position (mean of 19 substitutions), with catalogued mutation sites marked. (C) Top 20 most destabilising catalogued mutations.

2.6 Cryo-EM fibril structures reveal amyloid-selective binding sites

Comparison of the predicted mutant and wild-type monomers revealed limited global variation (TM-scores > 0.93), but cannot capture the conformational transition associated with fibril formation. The analysis was therefore extended to patient-derived cryo-EM TTR fibril structures: 6SDZ (V30M ATTR fibril, 2.97 Å resolution [44]) and 8ADE (ATTRwt fibril, 2.78 Å resolution [45]). These structures adopt a fold distinct from native TTR, with resolved N- and C-terminal segments within residues 11–123 arranged in a cross-β filament with a characteristic spearhead cross-section.

Relative solvent accessibility (RSA) was computed on the *complete deposited fibrillar assemblies*, comprising 11 chains for 6SDZ and 7 for 8ADE, and on the native 1ICT tetramer (chains A–D). This accounts for contacts within the deposited assemblies along and across the protofilament. Per-residue values were extracted for every chain and averaged (Methods). The N-terminal region adjacent to Cys10 showed a marked accessibility change (Site 1, residues 5–15). Pro11 was buried in the native tetramer (RSA = 0.055) but exposed in both fibrils (RSA = 0.576 in 6SDZ and 0.551 in 8ADE). Met13 (0.177 → 0.252/0.353) and Lys15 (0.082 → 0.244/0.259) also became more exposed (Fig. 8E). Mean RSA across residues 11–15 increased from 0.067 in native TTR to 0.236 in 6SDZ and 0.260 in 8ADE, a 3.5–3.9-fold increase (Fig. 8F). Leu12 and Val14 remained buried, placing the accessible surface around Pro11, Met13 and Lys15. Cys10 itself is unresolved in these structures, whose resolved N-terminal segments begin at residue 11. The candidate target is therefore an *N-terminal fibril-exposed epitope adjacent to the Cys10/PTM region*, rather than a modified-Cys10 epitope. The exposure profiles were similar across the two polymorphs, with a mean per-residue $|\Delta\text{RSA}|$ of 0.034 across residues 11–15. The analysis was then extended to the 30 patient-derived fibril structures available at the data-retrieval date: four ATTRwt cardiac fibrils from four patients (8E7D, 8G9R, 8GBR and 8E7H) [46]; four ATTRv-I84S cardiac folds (closed, open, absent and broken gate; 8TDN, 8TDO, 8E7E and 8E7J) [51]; the V30M vitreous fibril (7OB4) [51]; and nineteen biopsy-derived ATTRv fibrils spanning nine mutations (V30M, V30A, F33V, K35N, T59K, F64S, E61K, G83R and A97S; PDB 9W9J–9WA2) from muscle and vitreous samples [52].

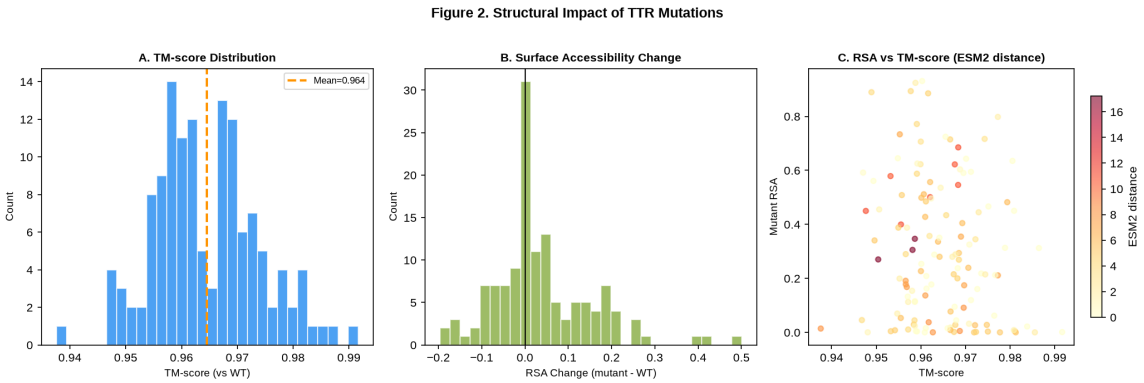


Figure 4: **Structural impact of TTR mutations.** (A) TM-score distribution for 133 mutations versus wild-type. (B) Distribution of surface accessibility changes (RSA mutant − RSA WT). (C) RSA versus TM-score, coloured by ESM2 pathogenicity distance.

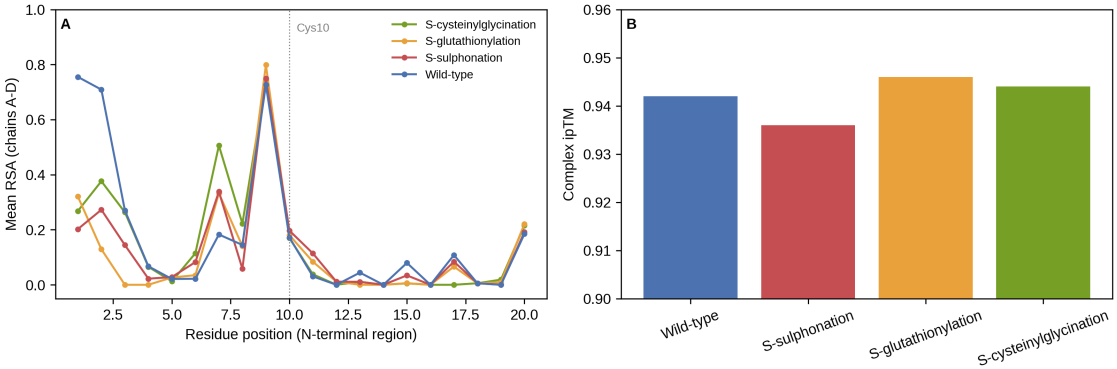


Figure 5: **Boltz-2 structural models of Cys10 post-translational modifications.** (A) Per-residue RSA of the N-terminal region (residues 1–20, mean of chains A–D) for the wild-type, Cys10-sulfonic-acid (oxidised), S-glutathionylated, and S-cysteinylglycinated tetramer models. (B) Complex ipTM of the four tetramer models. The sulfonic-acid model is a steric approximation and is chemically distinct from S-sulphonation (Methods).

Using a common Tien et al. normalisation reference for the extended panel, mean RSA across residues 11–15 was 0.17–0.46 in fibrils and 0.089 in the native tetramer (Table S1); Pro11 was the most exposed residue in nearly every structure. The original absolute threshold of mean RSA > 0.20 applies to the two-polymorph analysis. In the extended panel, the consistent finding is *increased relative exposure*, including the open-gate I84S fold 8TDO (0.168 versus 0.089 in native TTR), which falls below that absolute threshold. Although the I84S folds differ substantially in the polar-channel gate region [51], their N-terminal fragments remain exposed and conformationally close to the cardiac folds (Fig. 9B). Thus, increased N-terminal accessibility recurs across wild-type TTR and ten hereditary variants, three tissues and multiple fibril morphologies (Fig. 9).

The two comparator sites did not show the same accessibility pattern. Site 2 (V30M region, residues 26–36) became *more buried* in fibrils (native 0.203 → 0.133/0.142), providing no accessibility-based rationale for amyloid-selective targeting. Site 3 (Ser52 region, residues 48–58) was largely unresolved in the fibril structures; accessibility across the resolved residues 57–58 changed little (0.300 → 0.307/0.334). An amyloid-selective targetability score was defined as the change in mean RSA over resolved site residues (ΔRSA = fibril − native; Methods). Site 1 had the largest positive values (+0.169 and +0.193 for 6SDZ and 8ADE), whereas Sites 2 and 3 had negative or small positive values (Table 2). This accessibility-based score describes candidate antibody-target exposure rather than small-molecule druggability.

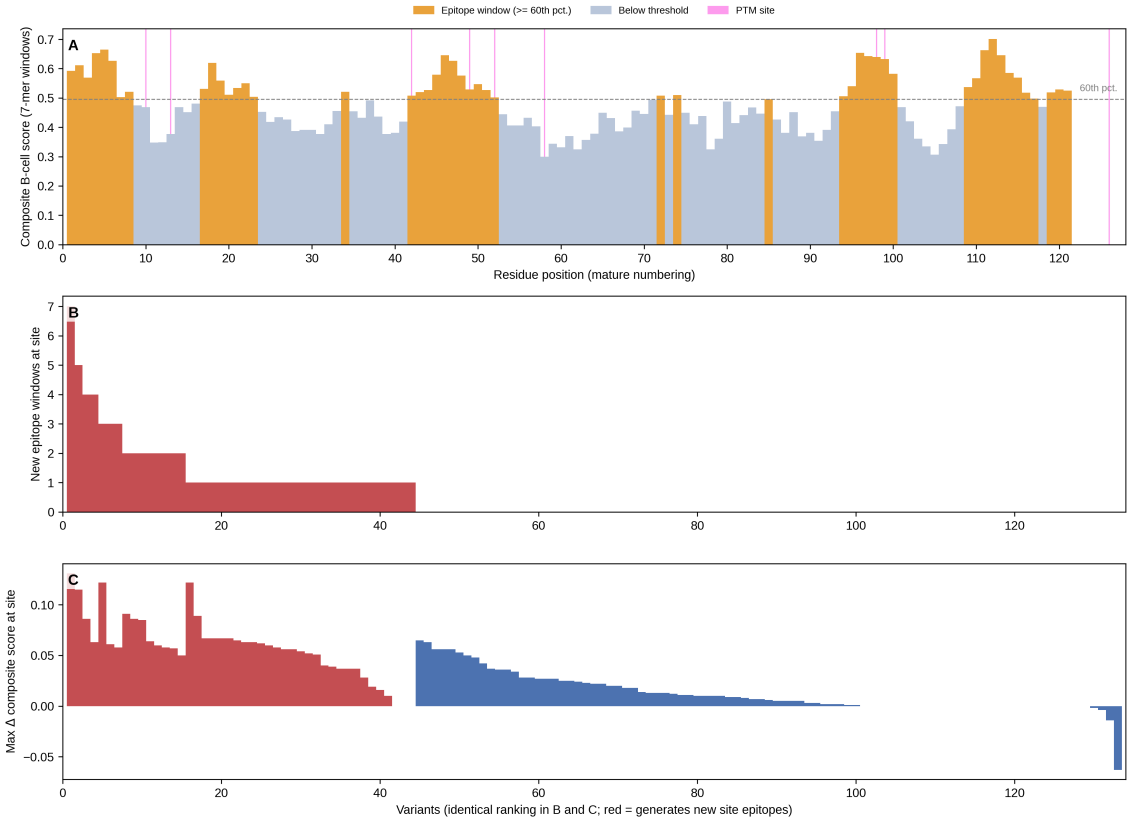


Figure 6: **Variant-specific B-cell epitope propensity changes.** (A) Composite B-cell propensity profile along the TTR sequence; orange bars denote windows above the sequence-specific 60th-percentile threshold and pink vertical lines indicate PTM sites. (B) Number of new mutation-overlapping windows per variant, with variants ordered by this count. (C) Maximum composite-score change at the mutated site per variant.

2.7 Generative antibody design targeting amyloid-selective sites

Binder format and design pipeline were selected for each candidate site. BoltzGen's nanobody-anything protocol [40] was used for Site 1 (Cys10-adjacent region, fibril-core RSA = 0.236–0.260) and Site 3 (Ser52 region), generating single-domain binders of 90–120 residues. Fifty intermediate designs per site passed through five stages (design → inverse folding → folding → analysis → filtering), yielding 10 final ranked candidates per site and 20 nanobody designs in total.

Site 2 (V30M region, residues 26–36) was retained as a non-amyloid-selective comparator. RFAntibody was used to generate variable-domain (Fv) designs through RFdiffusion backbone generation, ProteinMPNN CDR sequence assignment and RoseTTAFold2 (RF2) structural assessment. The pipeline models the hu-4D5-8 variable-domain framework with designed heavy- and light-chain CDRs; no Fc or constant domains are included. The resulting candidates are therefore termed Fv antibody designs throughout. RFdiffusion generated 20 antibody–target complex backbones using the antibody-finetuned checkpoint and hu-4D5-8 ScFv framework. CDR loop-length ranges were L1:8–13, L2:7, L3:9–11, H1:7, H2:6 and H3:5–13, with target hotspots T26–T36 on V30M TTR. ProteinMPNN assigned optimised sequences to all six CDR loops, replacing RFdiffusion's glycine placeholders. RF2 then predicted structures with 10 recycling iterations and scored predicted local distance difference test (pLDDT), predicted aligned error (pAE) and CDR root-mean-square deviation (RMSD) relative to the design backbone.

Sixteen of the 20 designs passed the filtering criteria (pAE < 10 and framework-aligned CDR RMSD < 2 Å). Mean RF2 pLDDT was 0.916 (range 0.910–0.930). The lowest-pAE design was site_2_design_9 (pAE = 6.21, CDR RMSD = 0.94 Å, pLDDT = 0.92). The lowest CDR RMSDs among passing designs were obtained for site_2_design_19 (0.78 Å) and site_2_design_16 (0.80 Å, pAE = 8.01). Four designs (2, 7, 8 and 12) were excluded because CDR RMSD exceeded 2 Å, indicating divergence between their RF2-predicted CDR conformations and design backbones.

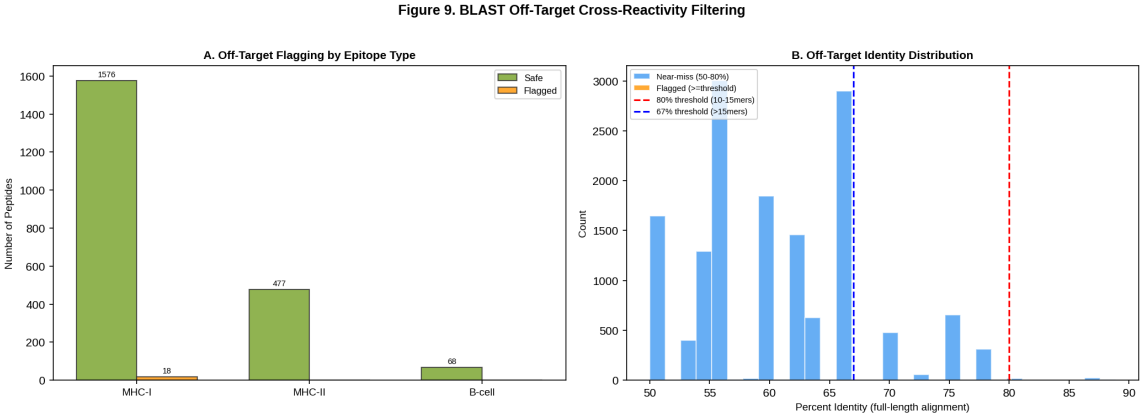


Figure 7: **Human-proteome sequence-similarity screening.** (A) Flagged and unflagged peptides by epitope type (the image labels unflagged peptides as "Safe, which does not imply experimental safety). (B) Identity distribution of full-length matches to non-TTR human proteins, with threshold lines.

Table 2: Native vs fibril accessibility comparison and amyloid-selective targetability. RSA values are means over complete assemblies, normalised with the Sander–Roupé maximum-ASA reference; Site 1 values use the resolved core (residues 11–15). Targetability score = ΔRSA (fibril mean RSA − native mean RSA) over resolved site residues.

Site	Residues	Native RSA	Fibril RSA	ΔRSA	Selectivity	Targetability
Site 1	5–15 (Cys10-adjacent)	0.067	0.236 / 0.260	+0.169/+0.193	Amyloid-selective	0.17–0.19
Site 3	48–58 (Ser52)	0.300	0.307 / 0.334	+0.007/+0.034	Non-selective	0.01–0.03
Site 2	26–36 (V30M)	0.203	0.133 / 0.142	−0.070/−0.061	Fibril-buried	<0

2.8 Boltz-2 complex prediction and ranking of all candidates

Boltz-2 provided an additional assessment of the designed antibody–TTR complexes using pTM, ipTM and pLDDT. These scores quantify confidence in predicted structures and interfaces, not binding affinity. All 20 nanobody designs were assessed. The highest-ranked candidate by composite score, site_1_design_29, had pTM 0.850, ipTM 0.746 and 10 predicted interface hydrogen bonds. The second-ranked candidate, site_1_design_10, had pTM 0.862, ipTM 0.739 and 12 predicted hydrogen bonds. The highest ipTM was obtained for site_1_design_19 (ipTM = 0.810, pTM = 0.886). Site 1 candidates were prominent among the highly ranked designs. These designs used a native-state surrogate; the subsequent fibril-targeted campaign is described below. Across the 20 designs, mean pTM was 0.724 (range 0.548–0.886) and mean ipTM was 0.489 (range 0.171–0.810).

Among the 10 Fv designs assessed with Boltz-2, the highest-ranked candidate by composite score, site_2_design_19, had pTM 0.918 and ipTM 0.881, with RF2 pAE 8.23 and CDR RMSD 0.78 Å. The highest interface confidence was obtained for site_2_design_6 (ipTM = 0.930, pTM = 0.948). Mean pTM was 0.860 (range 0.724–0.948) and mean ipTM was 0.803 (range 0.607–0.930). These values exceeded those of the nanobody designs, but the comparison is confounded by target site, binder format and design pipeline. The larger Fv interface and structure-based design procedure are possible explanations, rather than demonstrated causes, of this difference.

The Fv designs target Site 2, which becomes more buried in the fibril (native RSA 0.203 versus fibril RSA 0.133–0.142); the accessibility analysis therefore does not support amyloid selectivity at this site. V30M is nevertheless the most common pathogenic TTR mutation worldwide [4], motivating investigation of mutation-selective recognition. Residue 30 lies within the designed hotspot region T26–T36, but its participation in the predicted interfaces was not verified and no counter-prediction against wild-type Val30 TTR was performed. Mutation specificity consequently remains untested and would require direct comparison of binding to mutant and wild-type proteins, for example by surface plasmon resonance (SPR).

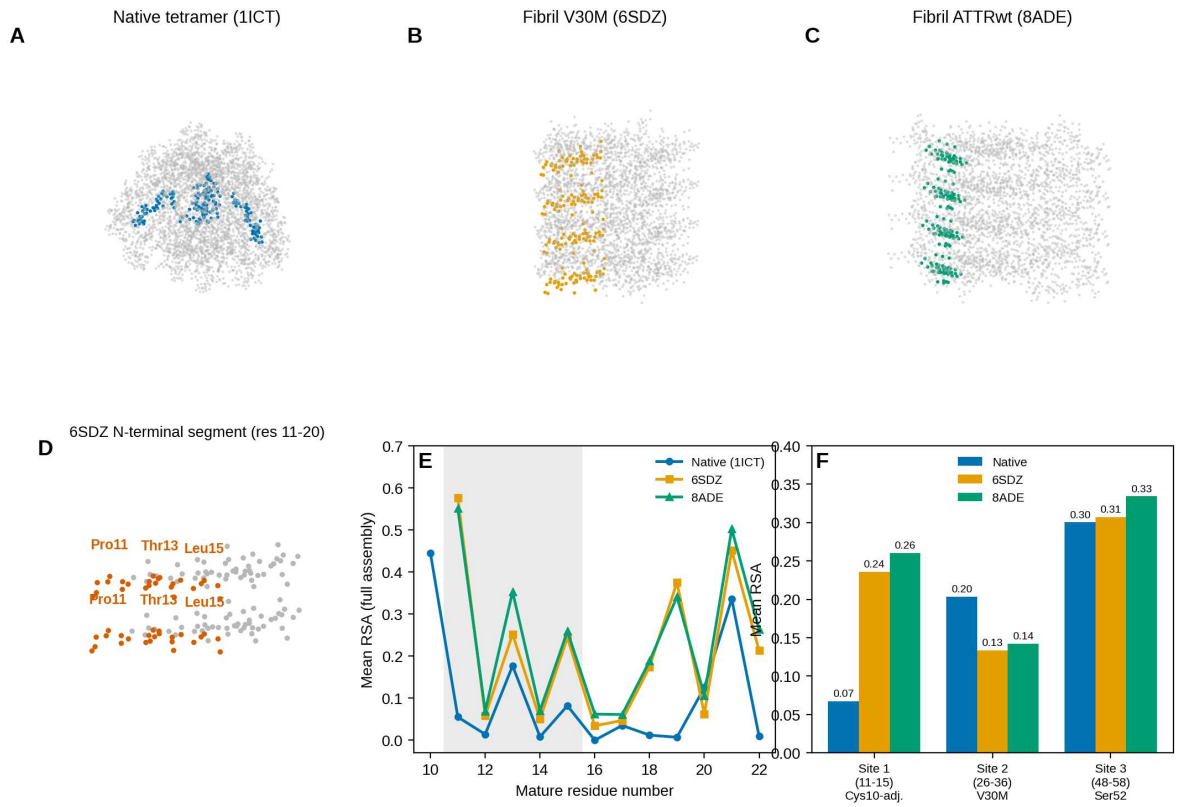


Figure 8: **Native-to-fibril accessibility remodelling identifies an amyloid-selective N-terminal epitope.** (A–C) Structural views of native TTR (1ICT), the V30M fibril (6SDZ) and the ATTRwt fibril (8ADE), with the N-terminal target region highlighted. (D) Enlarged view of the 6SDZ N-terminal segment. (E) Per-residue mean RSA, computed on complete assemblies and normalised using the Sander–Roupé maximum-ASA reference. (F) Mean RSA for the three candidate sites, using the resolved residues in each comparison.

2.9 Counter-prediction identifies construct-dependent N-terminal epitope engagement

The initial nanobody designs used a native-state surrogate monomer. A second BoltzGen campaign instead used chains A–D of the patient-derived V30M fibril structure 6SDZ, restricting the binding specification to mature residues 11–16, including Pro11, Met13 and Lys15. Ten intermediate designs yielded 5 final nanobodies (site_1_0, _2, _4, _5 and _7), with internal refolding ipTM values of 0.41–0.44.

The two highest-ranked designs (site1_0 and site1_2) underwent sequence-only Boltz-2 counter-prediction against constructs derived from four TTR states: 6SDZ, the alternative 8ADE fibril, the native 1ICT tetramer and the 1ICT monomer (Fig. 11). Interface confidence was high for both fibril-derived targets (site1_0: ipTM 0.763/0.715; site1_2: ipTM 0.823/0.884). Interface analysis placed site1_2 in contact with Pro11, Met13 and Lys15 in the 6SDZ-derived construct (24 interface residues spanning mature positions 11–60), and with Met13/Lys15 in the 8ADE-derived construct. Site1_0 contacted Pro11 in the 6SDZ-derived construct. In native-state constructs, the predicted contacts instead occurred at distal surfaces (tetramer: residues 62–102; monomer: residues 29–74), without Pro11/Met13/Lys15 contacts. Native-tetramer ipTM values remained high (0.78–0.80), so interface confidence alone did not distinguish the target states. The result is a difference in predicted epitope engagement, rather than evidence that native TTR cannot bind these candidates. Because the experimental fibril coordinates were not imposed during counter-prediction, recognition of the epitope in the experimental fibril geometry also remains to be established.

2.10 Vitreous-targeted designs predict cross-tissue epitope engagement

ATTR deposits occur in different tissues, including the heart and vitreous. Conformationally divergent exposed surfaces might therefore provide targets for tissue-selective binders. The 30-structure panel

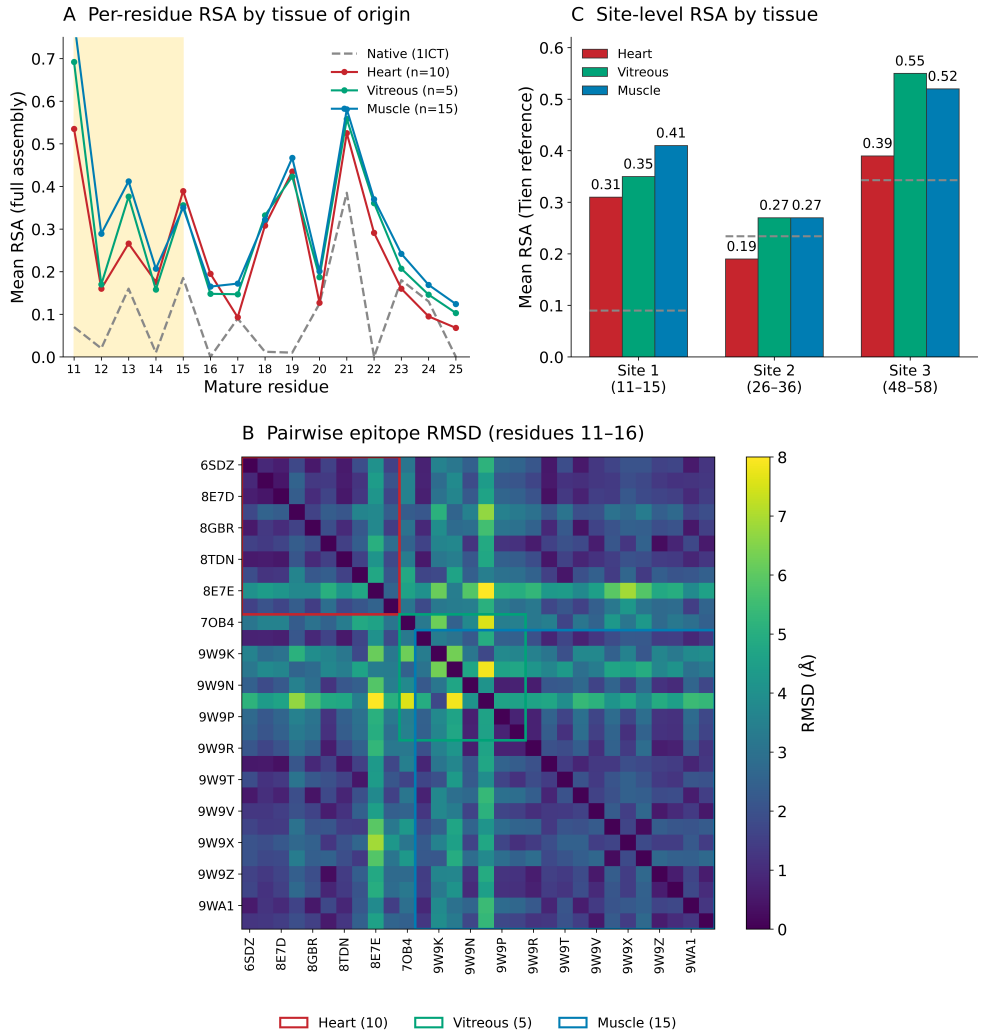


Figure 9: **The N-terminal exposure switch across the 30 analysed patient-derived TTR fibril structures.** (A) Per-residue mean RSA (full-assembly protocol, Tien et al. maximum-ASA reference) for residues 11–25, grouped by tissue of origin (heart, vitreous humour, skeletal muscle); the native tetramer is shown as a dashed reference. (B) Pairwise core-aligned Cα RMSD of the N-terminal epitope (residues 11–16) across all 30 fibril structures; tissue of origin marked by border colour. (C) Site-level mean RSA for the three candidate binding sites by tissue.

instead indicates that N-terminal exposure is broadly conserved (Fig. 9). Core-aligned Cα RMSD across residues 11–16 was 1.0 Å between the two cardiac fibrils and 1.7–4.3 Å between the vitreous F64S fibril and cardiac fibrils. A third BoltzGen campaign tested whether designs against the vitreous fibril would retain N-terminal contacts across tissue-derived constructs. Chains A–C of the F64S vitreous fibril 9W9N [52] were used, with binding restricted to mature residues 11–16 on each chain. Ten intermediate designs yielded 5 final nanobodies. The top design had design-to-target ipTM 0.324, refolded ipTM 0.342 and design pTM 0.858.

The two highest-ranked designs (f64s_nterm_3 and f64s_nterm_0) were counter-predicted against five constructs: the vitreous-derived 9W9N target, cardiac-derived 6SDZ and 8ADE targets, and native tetrameric and monomeric 1ICT targets (Fig. 12). Both designs contacted the intended N-terminal region in all three fibril-derived constructs. F64s_nterm_3 contacted Pro11–Lys15 in 9W9N (ipTM = 0.870), 6SDZ (0.887) and 8ADE (0.910); f64s_nterm_0 contacted Pro11–Lys15 or Pro11–Val14 across these constructs (ipTM 0.691–0.853). In both native-state constructs, predicted contacts occurred at distal surfaces (residues 27–90), without Pro11, Met13 or Lys15 contacts. For f64s_nterm_0, ipTM decreased to 0.389 in the native monomer, the lowest value in the panel. Thus, a campaign using a different tissue-derived fibril reproduced the predicted contrast in N-terminal epitope engagement, while also predicting cross-tissue recognition.

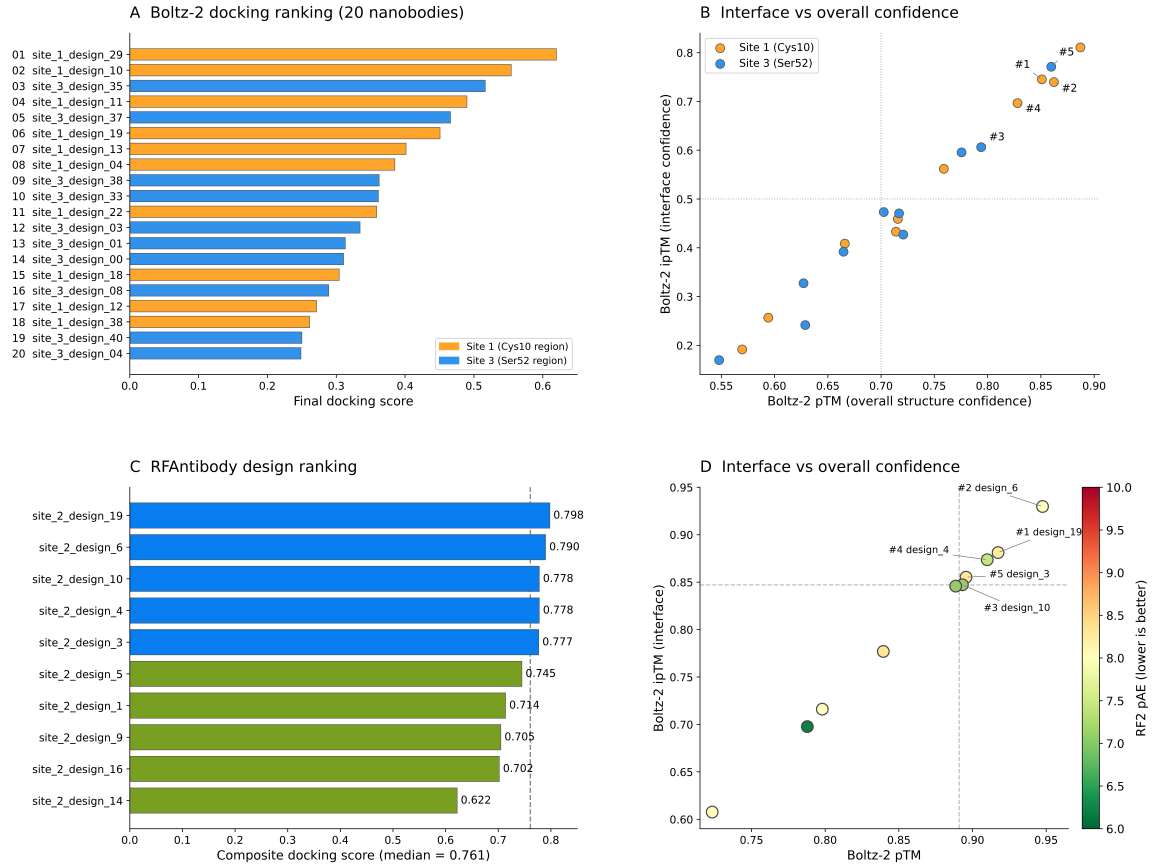


Figure 10: **Generative binder design and Boltz-2 complex prediction.** (A) Final confidence-based ranking for all 20 nanobody designs, coloured by target site (orange = Site 1/Cys10-adjacent, blue = Site 3/Ser52). (B) ipTM versus pTM scatter for nanobody designs, with the top 5 labelled. (C) Composite score ranking for 10 RFAntibody Fv designs, with the top 5 shown in blue. (D) ipTM versus overall pTM scatter for RFAntibody designs, coloured by RF2 pAE.

These predictions support cross-tissue recognition of the N-terminal region rather than tissue specificity. They are consistent with the broadly conserved N-terminal fragment (Leu12–Lys35), although conservation alone cannot establish binder cross-reactivity. A matched exploratory campaign targeted the polar-channel gate region (mature residues 58–66, including F64S) in 9W9N, a region that varies substantially among the I84S gate folds [51]. Five final designs were obtained, with lower design-to-target ipTM values (0.20–0.26) than in the N-terminal campaign (0.32–0.39). This is consistent with greater design difficulty at the relatively buried gate region (Fig. 9C), but does not establish that the region is intrinsically unsuitable for targeting. Tissue-selective binder design remains unresolved and may require other conformationally divergent, accessible surfaces.

2.11 Design quality control: format distributions, filter behaviour, and the H3 bottleneck

Fv designs had higher confidence scores than nanobodies: mean ipTM was 0.803 (range 0.607–0.930) versus 0.489 (range 0.171–0.810), and mean pTM was 0.860 (range 0.724–0.948) versus 0.724 (range 0.548–0.886) (Fig. 13A–C). This comparison is descriptive because the groups differ in paratope size, target site and design pipeline. It cannot isolate an effect of binder format or support therapeutic superiority.

The relationship between RF2 structural-quality metrics and Boltz-2 confidence was examined across the 10 assessed Fv designs. Seven RF2 metrics (pAE, interaction pAE, pLDDT, framework RMSD, CDR RMSD, H3 RMSD and L3 RMSD) were compared with four Boltz-2 metrics (pTM, ipTM, pLDDT and composite score), yielding 28 metric pairs and 56 tests using Pearson and Spearman coefficients. No statistically detectable association was found (all $p > 0.28$, $n = 10$). The strongest Pearson trend was RF2 pLDDT versus Boltz-2 ipTM ($r = -0.378$, $p = 0.28$), indicating a negative association in this small

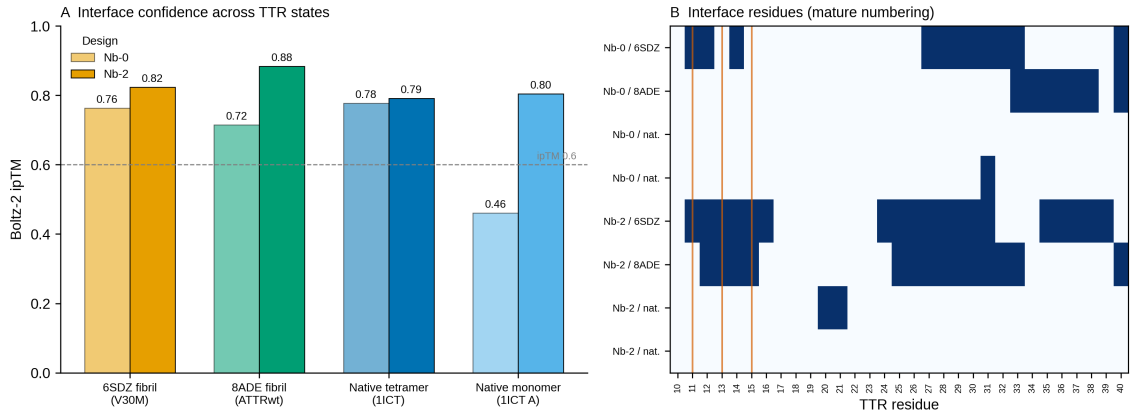


Figure 11: **Counter-prediction of fibril-designed nanobodies across TTR states.** (A) Boltz-2 interface confidence (ipTM) for the two lead designs against the 6SDZ fibril (design target), the 8ADE fibril (alternative polymorph), the native tetramer, and the native monomer. (B) Interface-residue map (mature numbering, residues 10–40) for each design–target pair; orange lines mark the hotspot residues Pro11, Met13, and Lys15. In fibril-derived constructs, predicted contacts include the N-terminal epitope; native-state constructs show distal contacts without hotspot engagement. Predictions were sequence-only and were not constrained to experimental target folds.

sample. Non-significant results do not establish independence or orthogonality between the metrics. RF2 assesses consistency with the design backbone, whereas Boltz-2 provides an additional predicted-complex assessment; the present data do not justify replacing either step with the other.

The 4 designs excluded by RF2 filtering (designs 2, 7, 8 and 12; CDR RMSD $>$ 2 Å) showed the greatest deviations in H3. Mean H3 RMSD was 4.75 Å (range 4.27–5.77) in excluded designs and 1.33 Å (range 0.49–3.12) in passing designs, a 3.6-fold difference. Other CDR loops (H1, H2, L1, L2 and L3) had RMSD values below 2 Å in both groups, implicating H3 as the principal source of CDR deviation. H3 length alone did not explain exclusion: excluded designs contained 6–13 residues, while design_11, with a 13-residue H3, passed. For CDR loops with variable lengths, no statistically detectable association with Boltz-2 interface confidence was found among the 10 assessed designs (all $p > 0.26$; Fig. 13, lower panels). Sequence–structure incompatibility is a possible explanation that requires further testing. Increasing ProteinMPNN sampling to 4–8 sequences per backbone could provide greater H3 sequence diversity in future campaigns.

3 Discussion

This study integrates native and patient-derived cryo-EM fibril structures to identify an exposed TTR amyloid surface and guide candidate-binder design. The principal structural finding is increased accessibility of the N-terminal region adjacent to Cys10 in the fibril panel. This change differs from those at the two comparator sites: the V30M region becomes more buried, while accessibility at the resolved portion of the Ser52 region changes little. The modification catalogue, saturation-mutagenesis landscape, PTM steric models and sequence-level epitope predictions provide supporting context; the native-to-fibril accessibility comparison and subsequent binder design constitute the main contribution.

The analysis highlights the value of comparing distinct conformational states when identifying candidate amyloid-selective surfaces. Predicted mutant and wild-type monomers retain similar global folds (TM-scores $>$ 0.93), whereas the native-to-fibril transition reorganises the TTR structure and exposes previously buried residues. Two methodological choices are important. First, accessibility should be evaluated on complete deposited fibrillar assemblies, because isolated chains overestimate exposure at intermolecular interfaces; finite deposited assemblies can nevertheless retain end effects. Second, comparison across polymorphs helps distinguish recurrent features from those specific to a single structure. The similar N-terminal exposure profiles in 6SDZ and 8ADE, and the increased exposure throughout the extended panel, support this region as a recurrent TTR amyloid feature within the analysed structure set. The same comparative strategy could be applied to other amyloid systems for which native and fibrillar structures are available.

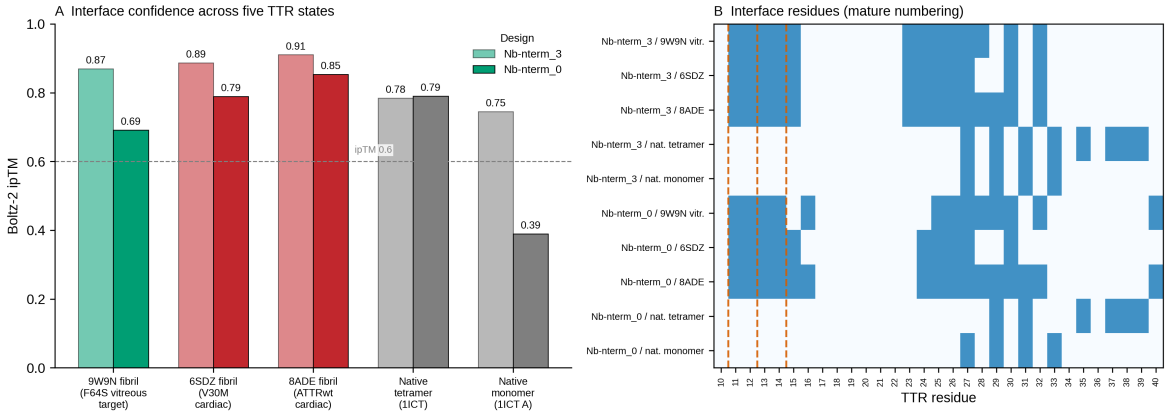


Figure 12: **Tissue-specificity counter-prediction of the F64S vitreous-fibril designs.** (A) Boltz-2 interface confidence (ipTM) for the two lead designs against five TTR states: the vitreous design target (9W9N, F64S), the two cardiac fibrils (6SDZ, V30M; 8ADE, ATTRwt), and the native tetramer and monomer (1ICT). (B) Interface-residue map (mature numbering, residues 10–40) for each design–target pair; dashed orange lines mark the hotspot residues Pro11, Met13, and Lys15. Predicted interfaces involve the N-terminal region in all three fibril-derived constructs and distal surfaces in both native-state constructs. Predictions were sequence-only and were not constrained to experimental target folds.

The candidate target is an N-terminal fibril-exposed epitope adjacent to the Cys10/PTM region. It is not a modified-Cys10 epitope: Cys10 is absent from the resolved N-terminal segments of the two principal fibril structures, which begin at residue 11. The predicted binder interfaces instead involve residues 11–15. The relationship to Cys10 chemistry is therefore indirect. PTMs may influence the transition to the amyloid state, while proteolysis and conformational remodelling may alter N-terminal accessibility. Unresolved residues alone do not establish proteolytic removal, and neither the processing history nor an effect of PTM state on the binder–fibril interface was tested here.

The designed binders remain computational candidates. Boltz-2 scores describe confidence in predicted structures and interfaces, rather than affinity. All complex counter-predictions were sequence-only, without experimental coordinates or structural restraints. Consequently, the fibril-derived target constructs were not constrained to retain the cryo-EM folds, and the observed contact patterns cannot demonstrate docking to experimental fibril geometry. Predicted interfaces engaged the intended region in fibril-derived constructs and distal surfaces in native-state constructs, but alternative native-state contacts mean that selective binding or absence of native-TTR binding cannot be inferred. Mutation specificity of the V30M-targeted Fv designs is also unresolved because residue 30 participation was not checked and wild-type counter-predictions were not performed. Three experimental steps would directly test the candidates: expression and developability assessment; SPR or biolayer interferometry (BLI) against preformed fibrils and native tetrameric TTR, with mutant and wild-type comparisons for V30M designs; and immunohistochemistry on patient-derived deposits. These measurements are prerequisites for interpreting the predictions as evidence of affinity, disease-state selectivity or tissue recognition.

The vitreous-fibril campaign further defines the scope of the approach. A binder that distinguished cardiac from ocular deposits could have diagnostic or therapeutic applications, but the analysed N-terminal region is exposed across tissues and relatively conserved across the fibril panel. Consistent with this pattern, vitreous-targeted candidates contacted the corresponding region in both vitreous- and cardiac-derived constructs. This supports a hypothesis of cross-tissue recognition within TTR amyloid, rather than established pan-amyloid binding. Whether such candidates could label or clear deposits in different organs would depend on affinity, tissue access, pharmacology and effector function, none of which was assessed. Conformationally divergent regions, such as the polar-channel gate [51], may offer alternative targets, although the matched gate-region campaign returned lower interface-confidence scores (ipTM 0.20–0.26). The available structures represent limited patient sampling and do not cover every disease compartment. In particular, central nervous system involvement and the distinct environment of choroid-plexus-derived TTR require dedicated investigation.

The contribution should also be considered alongside earlier amyloid-binder design and epitope-mapping studies. Fibril-capping miniproteins have been designed against tau, Aβ and α-synuclein [48], binders have been developed against amyloidogenic segments [49], and solvent-accessibility analysis has

informed individual TTR fibril studies [47]. The present work brings together a 30-structure TTR panel, a native-state accessibility reference and generative binder design, rather than establishing the broader concept of AI-designed amyloid binders. Several limitations remain. ThermoMPNN predictions concern monomer stability and do not capture tetramer-interface energetics or coupling between ligand binding and tetramer stability. The Cys10 models approximate adduct sterics without covalent geometry, while hormone-complex predictions assess structural accommodation rather than binding kinetics. Classical B-cell propensity scores are exploratory, and MHC predictions concern unmodified sequences overlapping PTM sites. Human-proteome similarity screening does not establish cross-reactivity or safety. Finally, MHC binding is allele-restricted, and immunogenicity depends on antigen processing, presentation and tolerance mechanisms not modelled here.

The workflow links modification annotation, predicted structural effects, native-to-fibril accessibility analysis and candidate-binder design. Its broader value lies in prioritising experimentally testable surfaces and sequences in protein-misfolding diseases with structural information for both native and aggregated states. Demonstrating conformation-selective binding will require structural assessment of the predicted complexes and direct experimental validation.

4 Methods

4.1 Data compilation

Residue numbers refer throughout to the 127-residue mature TTR sequence (UniProt P02766). In precursor numbering, the historically designated V30M variant corresponds to p.Val50Met. Filenames in the reused structure repository use precursor numbering (mature position + 20), whereas internal residue numbering follows the mature sequence.

The mature TTR sequence (127 amino acids) served as the reference. The 133 point mutations were retrieved from the repository accompanying Lomoio et al. [9]. PTM sites were compiled from UniProt annotations and the literature: Cys10 thiol modifications, oxidation, isoaspartate formation, proteolytic cleavage, N-glycosylation, phosphorylation and 4-carboxyglutamate formation from UniProt and mass-spectrometry studies [10, 12, 53, 11]; ubiquitination sites from proteostasis studies [10, 27]; SUMOylation at K126 from experimental reports [28]; tyrosine nitration from studies of nitrosative stress [25]; and carbonylation from oxidative-stress studies [10]. RNA isoforms were retrieved from Ensembl, and candidate m6A sites were identified using the RRACH consensus motif.

4.2 Saturation-mutagenesis stability prediction

ThermoMPNN [50], a graph neural network trained on the MegaScale dataset with transfer learning from ProteinMPNN, was used to predict $\Delta\Delta G$ for all possible single point mutations of the TTR monomer. The AlphaFold3 wild-type monomer structure (127 residues) served as input; site-saturation mutagenesis yielded 2,413 unique mutations (19 substitutions at each position). Negative $\Delta\Delta G$ values indicate stabilising mutations and positive values destabilising mutations. Per-variant structural metrics (mean pLDDT, residue RSA, TM-score versus wild-type) were computed from the 134 AlphaFold3 monomer structures (wild-type and 133 mutants) using Biopython's Shrake–Rupley solvent accessibility implementation and TMalign.

4.3 Cys10 PTM structural modelling

Three Cys10-associated modifications were approximated with Boltz-2 as bound-ligand complexes of the wild-type tetramer: cysteine sulfonic acid, specified by SMILES, for oxidation to sulfonic acid; glutathione (CCD GSH) for S-glutathionylation; and reduced cysteinylglycine, specified by SMILES, for S-cysteinylglycination. Cys10 oxidation to sulfonic acid (R–SO_3H) is chemically distinct from S-sulphonation (R–S–SO_3^-, S-sulfocysteine). Only the former was modelled. The bound-ligand approximation represents steric bulk near Cys10 and the thyroxine channel without specifying covalent geometry. Structures were predicted using the standard Boltz-2 pipeline and MSA server. Per-residue RSA in the N-terminal region was compared between wild-type and modified-complex models.

4.4 Ligand complex prediction

Triiodothyronine (T3) and thyroxine (T4) were placed into Boltz-2-predicted tetramer structures (wild-type and Cys10-modified) by joint complex prediction with Boltz-2, with all ligands specified as SMILES (the CCD cache lacked T4/T3 codes). Confidence metrics (ipTM, pTM, ligand pLDDT) were extracted from the output confidence records and compared across the wild-type and modified channels as measures of predicted structural accommodation, not of affinity or kinetics.

4.5 Structural modelling of mutations

Pre-computed AlphaFold3 structures (134 monomers and 134 tetramers) from Lomoio et al. [9] were reused. Surface accessibility (RSA) was computed using Shrake–Rupley as implemented in Biopython. Structural similarity was quantified by TM-score (TMalign, versus wild-type). Proteolytic cleavage fragments were generated by structure truncation. ESM2 pathogenicity predictions and stability data were integrated from the original study repository and from the ThermoMPNN saturation analysis described above.

4.6 Cryo-EM fibril structure analysis

The primary structural comparison used 6SDZ (V30M ATTR fibril, 2.97 Å [44]), 8ADE (ATTRwt fibril, 2.78 Å [45]) and the native TTR tetramer 1ICT, determined by X-ray crystallography, from the RCSB Protein Data Bank. RSA was computed using Biopython's Shrake–Rupley implementation with a 1.4 Å probe and Sander–Roupé maximum-ASA values for normalisation. Calculations used complete deposited assemblies: all 11 chains of 6SDZ, all 7 chains of 8ADE and chains A–D of 1ICT. Thus, contacts within the deposited assemblies along and across the protofilament were included. Per-residue RSA was extracted for each chain and averaged. The two fibril polymorphs were analysed independently. Exposure-profile similarity was quantified as the mean absolute per-residue RSA difference across the resolved Site 1 core (residues 11–15). For this primary comparison, candidate amyloid-selective exposure was defined as mean fibril RSA > 0.20 over the resolved site core, together with lower accessibility in native TTR. Targetability was quantified as ΔRSA (fibril − native) over matched resolved site residues. Pocket geometry was computed using ConvexHull on Cα atoms (scipy.spatial). Per-residue RSA values are provided in the Supplementary Data.

Extended 30-structure fibril panel: To test whether the N-terminal exposure generalises beyond the two original polymorphs, the identical full-assembly RSA protocol was applied to the 30 high-resolution patient-derived TTR fibril structures available on 3 October 2026: the four ATTRwt cardiac fibrils from four patients (8E7D, 8G9R, 8GBR, 8E7H) [46]; the four ATTRv-I84S cardiac gate folds (closed, open, absent, and broken gate; 8TDN, 8TDO, 8E7E, 8E7J) and the V30M vitreous fibril (7OB4) [51]; and the nineteen biopsy-derived ATTRv fibrils (9W9J–9WA2) spanning nine mutations (V30M, V30A, F33V, K35N, T59K, F64S, E61K, G83R, A97S) from muscle biopsies and vitreous humour [52]. For the cross-structure panel (Table S1, Fig. 9), per-chain RSA was normalised with the Tien et al. theoretical maximum-ASA reference [54]; the original 6SDZ/8ADE comparison (Fig. 8) retains the Sander–Roupé reference for continuity with the site-level analysis. Structures were grouped by tissue of origin as reported in the primary depositions: heart (10 structures), vitreous humour (5), and skeletal muscle (15). Pairwise N-terminal epitope divergence (Fig. 9B) was computed as the Cα RMSD of residues 11–16 after superposition on the fibril core (residues 58–123) by the Kabsch algorithm, with Cα atoms matched by mature residue number; the native tetramer (1ICT) was included as an outgroup reference.

4.7 Epitope prediction

B-cell: Linear epitopes were predicted using composite scoring (Parker hydrophilicity, Chou-Fasman turn propensity, Kolaskar-Tongaonkar antigenicity) with adaptive thresholding at the 60th percentile per sequence. For variant-specific epitope prediction, the composite profile was recomputed for each of the 133 mutant sequences via the IEDB B-cell epitope API (Parker, Chou-Fasman, Kolaskar-Tongaonkar methods) and compared position-wise with the wild-type profile; new epitope windows overlapping the mutated site were classified as variant-specific.

MHC-I: MHCflurry 2.0 (pan-specific model) predicted binding for 8–11mer peptides across 38 HLA-I alleles (10 supertypes). Strong binders: $\leq$0.5% rank; weak: 0.5–2% rank.

MHC-II: IEDB NetMHCIIpan predicted binding for 15mer peptides across 11 HLA-DR alleles. Strong binders: <1% rank; weak: 1–5% rank.

4.8 Human-proteome sequence-similarity screening

All unique candidate peptides were screened against the UniProt Swiss-Prot reviewed human proteome (20,431 proteins) using BLASTp with short-peptide-optimised parameters (word_size 2, evalue 10000, composition-based statistics disabled). TTR self-matches (P02766) were excluded. Thresholds were length-aware and set conservatively to exclude any near-exact match of immunoglobulin-contacting length: 100% identity for 8–9mers, ≥80% for 10–15mers, and ≥67% for >15mers, requiring full-length alignment coverage. This screen identifies sequence similarity only; it does not assess antibody cross-reactivity or immunological safety.

4.9 Antibody design

Nanobodies against the native-state surrogate: Nanobodies were designed using BoltzGen (nanobody-anything protocol, 50 designs per site, 10 final) [40]. The design target was a Boltz-2-predicted amyloidogenic TTR monomer (S52P surrogate structure); target-site residues were specified in the YAML design specification as residues 5–15 (Site 1) and 48–58 (Site 3).

Nanobodies against the fibrillar epitope: To design directly against the disease-state structure, a second BoltzGen campaign was performed (nanobody-anything protocol, 10 intermediate designs, 5 final) against the fibrillar target itself: chains A–D of the V30M patient-derived fibril structure 6SDZ, with the binding specification restricted to the fibril-exposed N-terminal segment (mature residues 11–16, containing Pro11, Met13, and Lys15) on each of the four stacked chains. The official RCSB mmCIF entry was used as target input, and three published nanobody frameworks (PDB 7EOW, 7XL0, 8COH) provided the CDR-grafting scaffolds. The design specification file is provided in the Supplementary Data.

Nanobodies against the vitreous F64S fibril: To test whether the pipeline supports tissue-specific binder design, a third BoltzGen campaign was performed (nanobody-anything protocol, 10 intermediate designs, 5 final) against chains A–C of 9W9N, the F64S ATTRv fibril from vitreous humour [52], with the binding specification restricted to the fibril-exposed N-terminal segment (mature residues 11–16, containing Pro11, Met13, and Lys15) on each of the three chains. The same three published nanobody frameworks (PDB 7EOW, 7XL0, 8COH) provided the CDR-grafting scaffolds. The F64S substitution (mature Ser64) lies in the polar-channel gate region, distant from the designed epitope, so the campaign probes tissue-of-origin discrimination at the N-terminus rather than mutation recognition.

Nanobodies against the gate region: As a tractability comparator, a matched fourth BoltzGen campaign (nanobody-anything protocol, 10 intermediate designs, 5 final) targeted the gate region of the polar channel on the same 9W9N target: binding was specified as mature residues 58–66 (containing the F64S site at position 64) on each of the three chains, with the same three nanobody frameworks (7EOW, 7XL0, 8COH). The design specification file is provided in the Supplementary Data.

Fv antibody designs: Variable-domain (Fv) antibody designs were generated using the RFAntibody pipeline (RFdiffusion → ProteinMPNN → RF2). RFdiffusion generated 20 antibody–target complex backbones using the antibody-finetuned checkpoint and the hu-4D5-8 ScFv framework, with CDR loop length ranges L1:8–13, L2:7, L3:9–11, H1:7, H2:6, H3:5–13 and hotspot residues T26–T36 on the V30M mutant TTR target. ProteinMPNN assigned optimised sequences to all six CDR loops using the interface design protocol. RF2 predicted structures from the designed sequences with 10 recycling iterations and scored each design by pLDDT, pAE, and CDR RMSD. Designs were filtered by pAE < 10 and framework-aligned CDR RMSD < 2 Å; 16 of 20 designs passed, and the 10 designs taken forward to Boltz-2 complex prediction were selected from the passing pool by RF2 quality rank (pAE and CDR RMSD). The per-design RF2 metrics and the selection ranking are available from the authors.

4.10 Boltz-2 complex prediction

Antibody–target complex structures were predicted using Boltz-2 [43] with the following parameters: `HF_HUB_OFFLINE=1 boltz predict -use_msa_server -num_workers 0 -no_kernels`. All complex predictions were *sequence-only*: the input files specify amino-acid sequences for each chain, with no structural templates, coordinates, or distance restraints of any kind. Consequently, the fibrillar targets are Boltz-2's own sequence-based models, and their geometry is *not* constrained to the experimental cryo-EM fibril folds; the disease-state contrast rests on the construct context (fibril-derived chain constructs versus full-length native chains), not on imposed fibril geometry. For nanobody designs, two-chain complexes (nanobody + TTR) were predicted. For RFAntibody designs, three-chain complexes (heavy chain + light chain + V30M TTR) were predicted. Confidence scores (pTM, ipTM, pLDDT) were extracted from the output JSON files. These are structural-confidence measures for the predicted complex and interface, not

binding-affinity estimates; they were used for ranking only. All input YAML files are provided in the Supplementary Data.

Counter-prediction against native and alternative fibril states: Selected lead nanobody sequences were predicted in complex with constructs derived from four TTR states: (a) 6SDZ chains A–D (V30M fibril, design target); (b) 8ADE chains A–D (ATTRwt fibril); (c) 1ICT chains A–D (native WT tetramer); and (d) 1ICT chain A (native WT monomer). Chain sequences were extracted from the experimental structures, with all chains of a state supplied as separate protein entities. Comparisons considered both interface confidence and contact composition. High ipTM alone was not interpreted as evidence of disease-state selectivity, particularly where alternative native-state interfaces were predicted. Interface residues were defined as TTR residues with any heavy atom within 4.5 Å of a nanobody atom; contacts involving Pro11, Met13 and Lys15 were inspected explicitly. As the predictions were sequence-only, these comparisons describe construct-dependent predicted interfaces rather than binding to fixed experimental conformations.

Tissue-specificity counter-prediction panel: For the F64S vitreous-fibril designs, the counter-prediction panel was extended to five TTR states to separate tissue-of-origin specificity from disease-state specificity: (a) the design target itself (9W9N chains A–C, F64S vitreous fibril), (b) the cardiac V30M fibril (6SDZ chains A–D), (c) the cardiac ATTRwt fibril (8ADE chains A–D), (d) the native WT tetramer (1ICT chains A–D), and (e) the native WT monomer (1ICT chain A). The two top-ranked designs by final BoltzGen rank were predicted against all five states. Tissue selectivity was read out as the contrast between vitreous-target engagement and cardiac-fibril or native-state engagement, combined with interface composition at Pro11/Met13/Lys15; a tissue-selective binder should engage the vitreous fibril at the designed epitope while docking elsewhere (or with lower interface confidence) on the cardiac fibrils, whose N-terminal epitope is conformationally distinct (Fig. 9B). The composite docking score for nanobodies combined BoltzGen design metrics with Boltz-2 confidence scores: $0.30 \times \text{design_iptm} + 0.25 \times \text{boltz2_iptm} + 0.20 \times \text{boltz2_ptm} + 0.15 \times \text{hbonds}/15 + 0.10 \times \text{design_ptm}$, with design_ptm on the 0–1 scale. The composite docking score for RFAntibody designs weighted interface confidence and incorporated RF2 quality metrics: $0.40 \times \text{boltz2_iptm} + 0.25 \times \text{boltz2_ptm} + 0.15 \times \text{boltz2_plddt} + 0.10 \times (1 - \text{rf2_pae}/10) + 0.10 \times (1 - \text{rf2_cdr_rmsd}/2)$.

4.11 Ranking and prioritisation

For T-cell candidates, composite scores were constructed as a weighted aggregation of normalised component scores: predicted MHC binding rank (lower is better), HLA supertype coverage, modification-site overlap, structural impact, clinical relevance, and experimental feasibility. Each component was min–max normalised to $[0, 1]$ before aggregation; flagged peptides received a 0.3 penalty to their composite score. The exact component weights were not retained in the archived pipeline outputs and are available from the authors. Component scores for all candidates are provided in the Supplementary Data.

4.12 Statistical analysis

Associations between RF2 and Boltz-2 metrics were assessed using Pearson and Spearman coefficients across $n = 10$ designs. The analysis comprised 28 metric pairs, each assessed by both coefficients (56 tests). No correction for multiple testing was applied; all reported p values were greater than 0.28. Given the small sample, non-significant results were interpreted as an absence of statistically detectable association, rather than evidence of independence. Comparisons between binder formats were descriptive because target site, format and design pipeline were confounded.

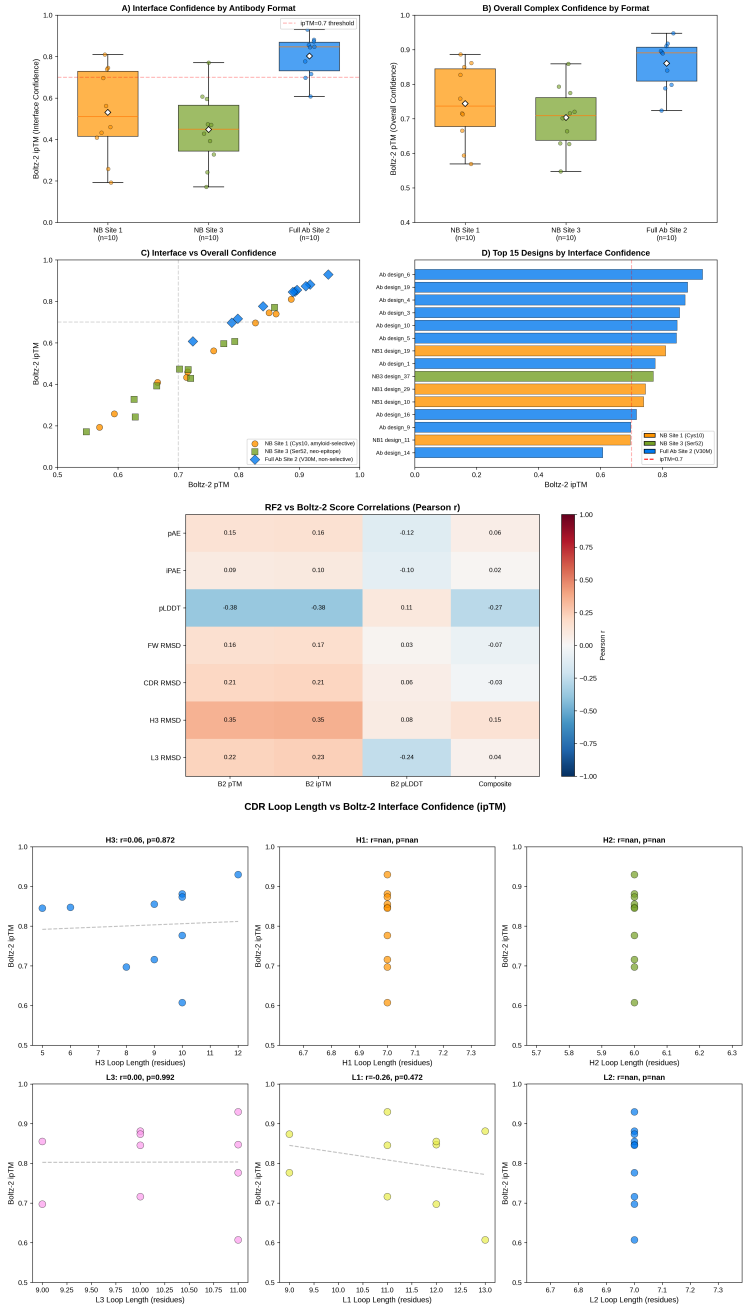


Figure 13: **Design quality control.** (A,B) Distributions of ipTM and pTM by binder format and target site. (C) ipTM versus pTM, coloured by group. (D) Ranking by interface confidence. The unlettered middle heatmap shows Pearson correlations between RF2 structural metrics and Boltz-2 metrics (all $p > 0.28$, $n = 10$). The lower scatterplots show CDR-loop lengths versus Boltz-2 ipTM for the assessed Fv designs; correlations are undefined for invariant loop lengths. Comparisons between formats are descriptive.

5 Supplementary material

Table S1: N-terminal site exposure (mean RSA over mature residues 11–15, full-assembly Shrake–Rupley, identical protocol and Tien et al. maximum-ASA reference [54] for all structures) across the 30 patient-derived TTR fibril structures in the analysed panel and the native tetramer. Values in this table are not directly comparable to the Sander–Roupé-normalised values in Table 2. Genotypes span wild-type (ATTRwt) and hereditary variants (V30M, I84S, F64S, A97S, E61K, T59K, G83R, V30A, K35N, F33V); tissues span heart, skeletal muscle, and vitreous humour.

PDB	Description	Source	RSA (11–15)
1ICT	Native tetramer (reference)		0.089
6SDZ	V30M fibril	heart	0.253
8ADE	ATTRwt fibril	heart	0.279
8E7D	ATTRwt patient 1	heart	0.297
8G9R	ATTRwt patient 2	heart	0.395
8GBR	ATTRwt patient 3	heart	0.335
8E7H	ATTRwt patient 4	heart	0.295
8TDN	I84S closed gate	heart	0.257
8TDO	I84S open gate	heart	0.168
8E7E	I84S absent gate	heart	0.329
8E7J	I84S broken gate	heart	0.322
7OB4	V30M vitreous	vitreous	0.268
9W9J	V30M type I	muscle biopsy	0.379
9W9K	V30M type II	muscle biopsy	0.374
9W9L	V30M type III	muscle biopsy	0.458
9W9N	F64S type I	vitreous	0.387
9W9O	F64S type II	vitreous	0.362
9W9P	F64S type III	vitreous	0.376
9W9Q	F64S type IV	vitreous	0.359
9W9R	A97S type I	muscle biopsy	0.403
9W9S	A97S type II	muscle biopsy	0.382
9W9T	A97S type III	muscle biopsy	0.400
9W9U	E61K	muscle biopsy	0.424
9W9V	T59K	muscle biopsy	0.427
9W9W	G83R type II	muscle biopsy	0.349
9W9X	G83R type I	muscle biopsy	0.368
9W9Y	G83R type II	muscle biopsy	0.369
9W9Z	V30A type I	muscle biopsy	0.451
9WA0	V30A type II	muscle biopsy	0.423
9WA1	K35N	muscle biopsy	0.434
9WA2	F33V	muscle biopsy	0.413

Table S2: Top 10 prioritised epitope candidates. All pass human-proteome sequence-similarity screening.

Type	Epitope	Source	Best allele	% Rank	Score	Screen
MHC-I	AINVAVHAF	V32A	B*46:01	0.06	0.82	Pass
MHC-II	RRYTIAALMSPYSYS	L111M	DRB1*08:02	0.28	0.79	Pass
MHC-I	SESEELHGL	G53E	B*40:01	0.004	0.79	Pass
MHC-I	AINVAGHVF	V30G	B*46:01	0.13	0.79	Pass
MHC-I	ESVEGIYKV	F64S	A*69:01	0.006	0.79	Pass
MHC-I	AALLSPHSY	Y114H	B*46:01	0.02	0.79	Pass
MHC-I	RESGELHGL	S50R	A*02:01	0.02	0.79	Pass
MHC-I	VEIDTKYYW	S77Y	A*23:01	0.01	0.79	Pass
MHC-II	RYTIAALMSPYSYST	L111M	DRB1*08:02	0.25	0.79	Pass
MHC-I	DTWEPSASGK	F44S	A*26:01	0.07	0.78	Pass

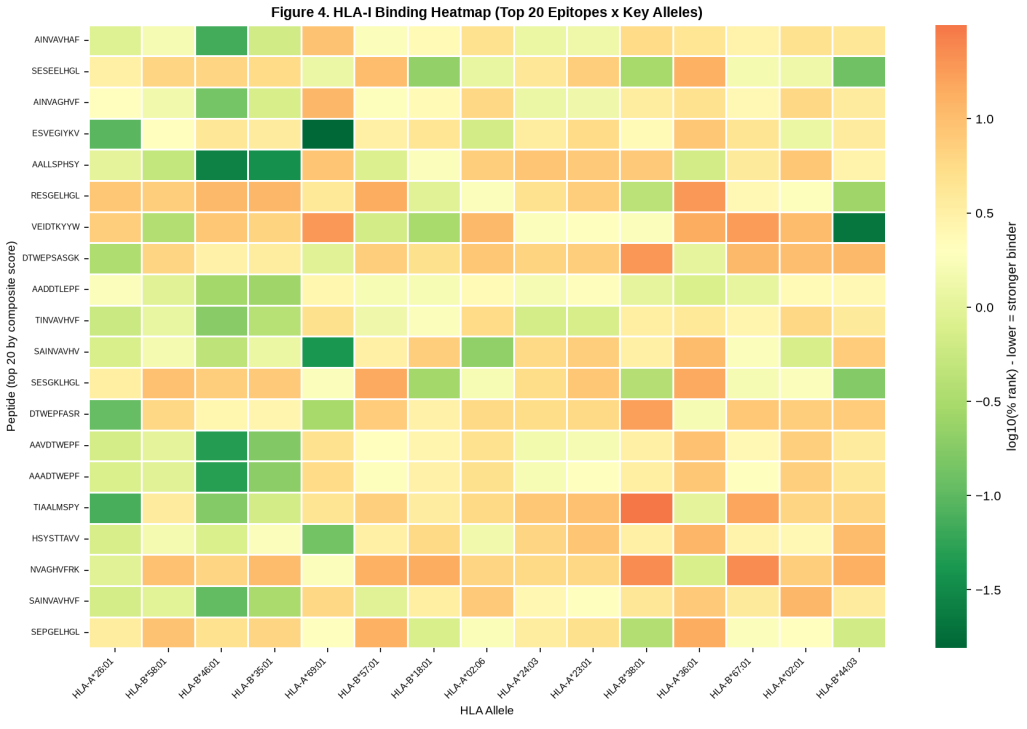


Figure S1: **HLA-I binding of top candidates.** Predicted binding percentile ranks for the top 20 candidates across selected HLA alleles, displayed on the logarithmic scale shown in the colour bar. Darker green indicates a lower rank and stronger predicted binding.

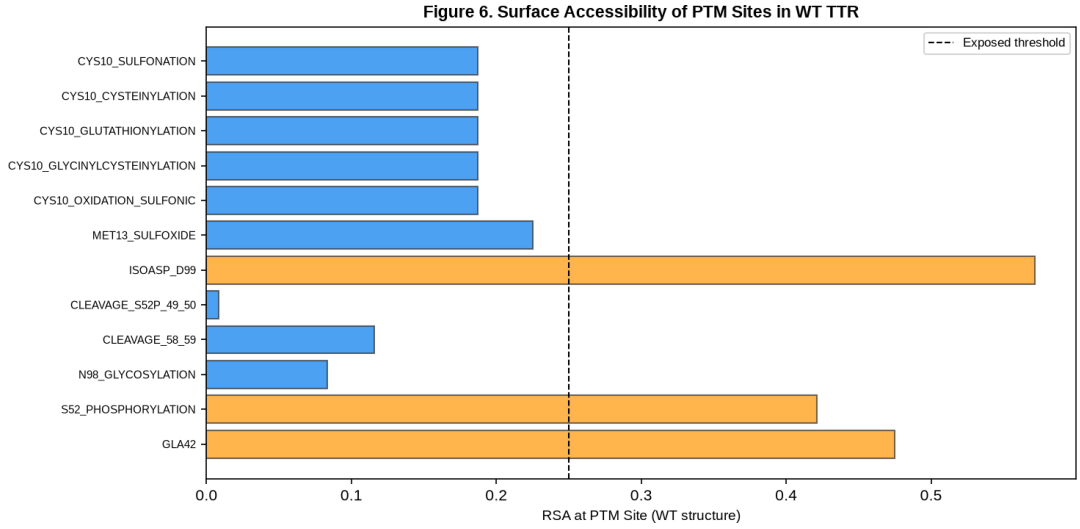


Figure S2: **PTM-site accessibility in the native tetramer.** Per-site RSA for the catalogued PTM positions, with buried sites highlighted.

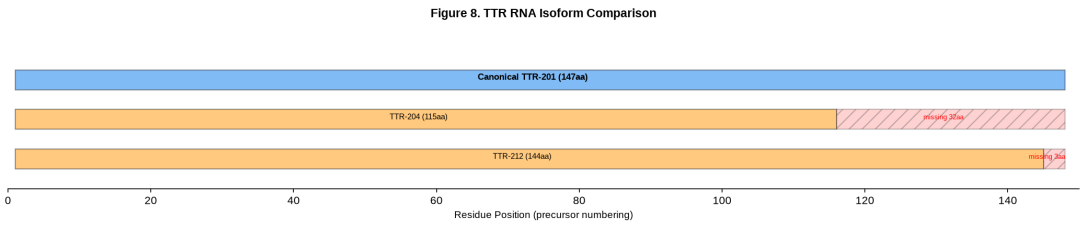


Figure S3: **TTR RNA isoforms.** Predicted protein lengths and altered segments for the three RNA isoforms, shown in precursor numbering.

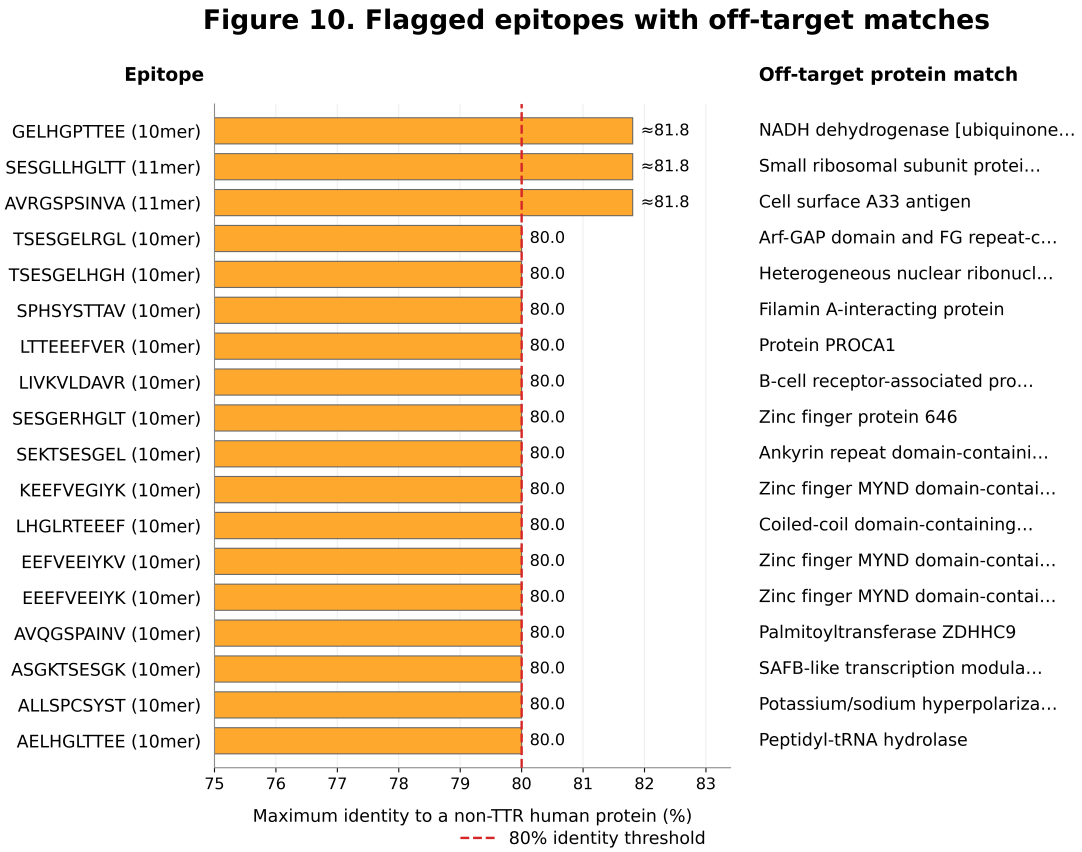


Figure S4: **Peptides flagged by human-proteome sequence-similarity screening.** Maximum full-length sequence identity of the 18 flagged peptides to non-TTR human proteins, with the corresponding protein matches. The dashed line marks the 80% identity threshold for peptides of these lengths.

Author contributions

Ugo Lomoio: Software, Investigation. **Valentina Carbonari:** Software. **Pietro Hiram Guzzi:** Conceptualisation, Software, Investigation. **Pietro Lió:** Conceptualisation. **Pierangelo Veltri:** Funding acquisition, Project administration. **Paola Roncada:** Supervision (biological guidance). **Andrea Urbani:** Supervision (biological guidance).

Competing interests

The authors declare no competing interests. [Placeholder to be confirmed before submission.]

Correspondence

Correspondence and requests for materials should be addressed to Pietro Hiram Guzzi (`[email placeholder]`).

Data availability

The TTR mutation list and pre-computed AlphaFold3 structures are available at `https://github.com/UgoLomoio/ttr_mutations`. Cryo-EM structures were retrieved from the RCSB PDB (accessed 3 October 2026): the native tetramer (1ICT) and the 30 patient-derived fibril structures 6SDZ, 8ADE, 8E7D, 8G9R, 8GBR, 8E7H, 8TDN, 8TDO, 8E7E, 8E7J, 7OB4, 9W9J, 9W9K, 9W9L, 9W9N, 9W9O, 9W9P, 9W9Q, 9W9R, 9W9S, 9W9T, 9W9U, 9W9V, 9W9W, 9W9X, 9W9Y, 9W9Z, 9WA0, 9WA1, and 9WA2. The following data files generated in this study are provided in `https://github.com/UgoLomoio/ttr-fibril-epitopes`: saturation-mutagenesis $\Delta\Delta G$ predictions (thermompnn_ssm.csv, thermompnn_cataloged.csv), per-variant structural metrics (structural_metrics.csv), per-variant epitope profiles (epitope_profiles.csv, epitope_positions.json), full-assembly fibril RSA values (rsa_full_assembly_sites.csv), PTM model metrics (ptm_metrics.csv, ptm_nterm_rsa.csv), ligand complex-prediction summary (docking_summary.csv), the expanded 30-structure RSA panel with per-residue values (rsa_expanded_panel.json), the pairwise N-terminal RMSD matrix and structure order (nterm_pairwise_rmsd.npy, nterm_pairwise_rmsd_order.json), BoltzGen design specifications (design_fibril_site1.yaml, design_f64s_nterm.yaml, design_f64s_gate.yaml), candidate binder sequences (final_nanobody_sequences.json, f64s_nanobody_sequences.json, f64s_gate_nanobody_sequences.json), and counter-prediction interface and scoring data (interface_residues.json, f64s_interface_residues.json, counter_pred_scores.json, f64s_counter_pred_scores.json). The per-design RF2 quality metrics and exact T-cell-prioritisation weights are available from the authors.

Code availability

Analyses were performed using ProteoformAnalyzer (`https://github.com/UgoLomoio/proteoform_analyzer`), including ThermoMPNN-based stability assessment, structural impact analysis of post-translational modifications and missense mutations, Boltz-2 structure prediction, epitope prediction, BoltzGen-based design, and RFAntibody design.

References

[1] M. D. Benson. Pathogenesis of transthyretin amyloidosis. *Amyloid*, 19, 2012.

[2] Mitsuharu Ueda. Transthyretin: Its function and amyloid formation. *Neurochemistry International*, 2022.

[3] S. Sebastian and J. Smith. Biology and function of transthyretin. *Cellular and Molecular Life Sciences*, 75:149–163, 2018.

[4] Zaida L. Almeida, D. C. Vaz, and Rui M. M. Brito. Transthyretin mutagenesis: impact on amyloidogenesis and disease. *Critical Reviews in Clinical Laboratory Sciences*, 2024.

[5] A. Gonzalez-Duarte and A. Ulloa-Aguirre. A brief journey through protein misfolding in transthyretin amyloidosis (attr amyloidosis). *International Journal of Molecular Sciences*, 22, 2021.

[6] F. L. Ruberg and Mathew S. Maurer. Cardiac amyloidosis due to transthyretin protein. *JAMA*, 2024.

[7] A. Porcari, M. Fontana, and J. Gillmore. Transthyretin cardiac amyloidosis. *Cardiovascular Research*, 2022.

[8] V. Plante-Bordeneuve. The v30m mutation in transthyretin amyloidosis. *Orphanet Journal of Rare Diseases*, 16:115, 2021.

[9] Ugo Lomoio, Valentina Carbonari, Federico Manuel Giorgi, Francesco Ortuso, Pietro Lio, Pierangelo Veltri, and Pietro Hiram Guzzi. Integrative structural profiling and ligand optimisation across the transthyretin mutational landscape. *npj Systems Biology and Applications*, 11:104, 2025.

[10] C. Sanguinetti, M. Minniti, V. Susini, et al. The journey of human transthyretin: Synthesis, structure stability, and catabolism. *Biomedicines*, 10, 2022.

[11] Lei Zhao, Joel Buxbaum, and Natalia Reixach. Age-related oxidative modifications of transthyretin modulate its amyloidogenicity. *Biochemistry*, 52, 2013.

[12] M. Vilà-Rico, S. A. Contesse, J. E. Barcena Llona, et al. Mass spectrometry analysis of transthyretin (ttr) post-translational modifications (ptms) in hereditary attr. *Orphanet Journal of Rare Diseases*, 10, 2015.

[13] B. Petersen and N. Blom. Post-translational modifications and their impact on protein function. *Protein Science*, 28:913–921, 2019.

[14] D.B. Friedman and T.E. Johnson. Protein modifications and aging. *Mechanisms of Ageing and Development*, 150:44–49, 2015.

[15] E.R. Stadtman. Protein oxidation and aging. *Free Radical Research*, 40:1250–1254, 2006.

[16] A. Krisko and M. Radman. Proteome instability in aging. *Cellular and Molecular Life Sciences*, 70:4685–4697, 2013.

[17] F.U. Hartl and M. Hayer-Hartl. Protein quality control and aging. *Nature Reviews Molecular Cell Biology*, 12:674–685, 2011.

[18] Y. Liu and G. Brede. Oxidative modifications destabilize transthyretin. *Redox Biology*, 21:101094, 2019.

[19] J.A. Rodriguez and D.S. Eisenberg. Post-translational modifications in amyloid deposits. *Journal of Molecular Biology*, 432:1225–1234, 2020.

[20] T. Miyagawa and M. Nagata. Age-dependent changes in transthyretin ptms and amyloidosis. *International Journal of Molecular Sciences*, 23:5578, 2022.

[21] H. Wang and Z. Chen. Role of aging in modulating transthyretin amyloidogenesis. *Frontiers in Aging Neuroscience*, 15:1056376, 2023.

[22] W.E. Balch and R.I. Morimoto. Age-related decline in proteostasis and its implications. *Nature*, 30:443–451, 2008.

[23] M. Mari and D. Pagnozzi. Influence of aging on post-translational modifications. *Aging Cell*, 17:e12702, 2018.

[24] Andrea Henze, Thomas Homann, Mustafa Serteser, Ozge Can, Ozlem Sezgin, Abdurrahman Coskun, Ibrahim Unsal, Florian J. Schweigert, and Aysel Ozpinar. Post-translational modifications of transthyretin affect the triiodonine-binding potential. *Journal of Cellular and Molecular Medicine*, 19:359–370, 2015.

[25] Meesha Sharma, Sheeza Khan, Safikur Rahman, and Laishram Rajendrakumar Singh. The extracellular protein, transthyretin is an oxidative stress biomarker. *Frontiers in Physiology*, 2019.

[26] Jonathan S. Kingsbury, Thomas M. Laue, Elena S. Klimtchuk, Roger Théberge, Catherine E. Costello, and Lawreen H. Connors. The modulation of transthyretin tetramer stability by cysteine 10 adducts and the drug diflunisal. *Journal of Biological Chemistry*, 283:11887–11896, 2008.

[27] Ridwan Benatunde Ibrahim, Ssu-Yu Yeh, Kon-Ping Lin, et al. Cellular secretion and cytotoxicity of transthyretin mutant proteins underlie late-onset amyloidosis and neurodegeneration. *Cellular and Molecular Life Sciences*, 2019.

[28] Elżbieta Wieczorek, Sylwia Kędracka-Krok, Katarzyna Soł tys, Urszula Jankowska, Rafał Hoł ubowicz, Justyna Seliga, and Andrzej Ożyhar. Is transthyretin a regulator of ubc9 sumoylation? *PLOS ONE*, 2016.

[29] Elzbieta Wieczorek and Andrzej Ozyhar. Transthyretin: From structural stability to osteoarticular and cardiovascular diseases. *Cells*, 10, 2021.

[30] Amira Zaroui, Catherine Lafont, Mounira Kharoubi, et al. Men and women differ with regard to the prevalence, phenotype, and prognosis of wild-type transthyretin amyloid cardiomyopathy. *Amyloid*, 2025.

[31] S. Vilches, Maria Martinez-Avial, Irene Mendez, et al. Sex differences in transthyretin cardiac amyloidosis: Unraveling the complexities. *Current Heart Failure Reports*, 2024.

[32] N. Mora-Ayestaran, A. Dispenzieri, A. V. Kristen, et al. Age- and sex-related differences in patients with wild-type transthyretin amyloidosis: Insights from thaos. *JACC: Advances*, 2024.

[33] Aubin Michalon, Andreas Hagenbuch, Christoph Huy, et al. A human antibody selective for transthyretin amyloid removes cardiac amyloid through phagocytic immune cells. *Nature Communications*, 12, 2021.

[34] J. Higaki, A. Chakrabartty, N. J. Galant, et al. Novel conformation-specific monoclonal antibodies against amyloidogenic forms of transthyretin. *Amyloid*, 2016.

[35] Janett Koppen, Martin Kleinschmidt, Markus Morawski, et al. Identification of isoaspartate-modified transthyretin as potential target for selective immunotherapy of transthyretin amyloidosis. *Amyloid*, 2024.

[36] A. Teixeira and M. Saraiva. Selective recognition of human small transthyretin aggregates by a novel monoclonal antibody. *Amyloid*, 2022.

[37] Giampaolo Merlini and Vittorio Bellotti. Molecular mechanisms of amyloidosis. *New England Journal of Medicine*, 349(6):583–596, 2003.

[38] Laura M Dember, Philip N Hawkins, Bouke PC Hazenberg, Peter D Gorevic, Giampaolo Merlini, Irena Butrimiene, Avi Livneh, Olga Lesnyak, Xavier Puéchal, Helen J Lachmann, et al. Eprodisate for the treatment of renal disease in aa amyloidosis. *New England Journal of Medicine*, 356(23):2349–2360, 2007.

[39] Giampaolo Merlini. A step forward in solving amyloidosis, 2023.

[40] Hannes Stark, Felix Faltings, MinGyu Choi, Yuxin Xie, Eunsu Hur, Timothy J. O'Donnell, Anton Bushuiev, Talip Uçar, Saro Passaro, Weian Mao, Mateo Reveiz, et al. Boltzgen: Toward universal binder design. *bioRxiv*, 2025. PMCID: PMC12697729.

[41] J. L. Watson et al. De novo design of protein structure and function with rfdiffusion. *Nature*, 620, 2023.

[42] J. Dauparas et al. Robust deep learning–based protein sequence design using proteinmpnn. *Science*, 378, 2023.

[43] Saro Passaro, Gabriele Corso, Jeremy Wohlwend, Mateo Reveiz, Stephan Thaler, Vignesh Ram Somnath, Noah Getz, Tally Portnoi, Julien Roy, Hannes Stark, David Kwabi-Addo, Dominique Beaini, Tommi Jaakkola, and Regina Barzilay. Boltz-2: Towards accurate and efficient binding affinity prediction. *bioRxiv*, page 2025.06.14.659707, 2025.

[44] M. Schmidt, S. Wiese, V. Adak, J. Engler, S. Agarwal, G. Fritz, P. Westermark, M. Zacharias, and M. Fändrich. Cryo-em structure of a transthyretin-derived amyloid fibril from a patient with hereditary attr amyloidosis. *Nature Communications*, 10:5008, 2019.

[45] M. Steinebrei, J. Gottwald, J. Baur, C. Rocken, U. Hegenbart, S. Schonland, and M. Schmidt. Cryo-em structure of an attrwt amyloid fibril from systemic non-hereditary transthyretin amyloidosis. *Nature Communications*, 13:6398, 2022.

[46] B. A. Nguyen, V. Singh, S. Afrin, P. Singh, M. Pekala, Y. Ahmed, R. Pedretti, J. Canepa, A. Lemoff, B. Kluve-Beckerman, P. M. Wydorski, F. Chhapra, and L. Saelices. Cryo-em confirms a common fibril fold in the heart of four patients with attrwt amyloidosis. *Communications Biology*, 7:905, 2024.

[47] Jun Yu, Xuefeng Zhang, Sandra Pinton, Elena Vacchi, Andrea Cavalli, Matteo Pecoraro, Giorgia Melli, Andreas Boland, et al. Structure of attrv-f64s fibrils isolated from skin tissue of a living patient. *Nature Communications*, 17:781, 2025.

[48] Kevin A. Murray, Carolyn J. Hu, Sarah L. Griner, Hope Pan, Jeannette T. Bowler, Romany Abskharon, Gregory M. Rosenberg, Xinyi Cheng, et al. De novo designed protein inhibitors of amyloid aggregation and seeding. *Proceedings of the National Academy of Sciences*, 119:e2206240119, 2022.

[49] Danny D. Sahtoe, Ewa A. Andrzejewska, Hannah L. Han, Enrico Rennella, Matthias M. Schneider, Georg Meisl, Maggie Ahlrichs, Justin Decarreau, et al. Design of amyloidogenic peptide traps. *Nature Chemical Biology*, 20:981–990, 2024.

[50] Henry Dieckhaus, Michael Brocidiacono, Nicholas Z. Randolph, and Brian A. Kuhlman. Transfer learning to leverage larger datasets for improved prediction of protein stability changes. *Proceedings of the National Academy of Sciences*, 121(6):e2314833121, 2024.

[51] Binh An Nguyen, Virender Singh, Shumaila Afrin, Preeti Singh, Maja Pekala, Yasmin Ahmed, Rose Pedretti, Jacob Canepa, Andrew Lemoff, Barbara Kluve-Beckerman, Pawel M. Wydorski, Farzeen Chhapra, and Lorena Saelices. Structural polymorphism of amyloid fibrils in attr amyloidosis revealed by cryo-electron microscopy. *Nature Communications*, 15:581, 2024.

[52] Yuxin Zheng, Jiawei Liang, Zhenyu Li, Yixiao Liu, Xujun Chu, Shaochong Zhang, Wenjuan Wang, Jionglin Bao, Boyu Liu, Conghui Ma, Guowei Yin, Jianwen Deng, Wei Chi, Lingchao Meng, and Yang Shi. Cryo-em structures of biopsy-derived ttr fibrils in hereditary transthyretin amyloidosis. *Nature Communications*, 17, 2026.

[53] A. Lim, T. Prokaeva, M. E. McComb, et al. Identification of s-sulfonation and s-thiolation of a novel transthyretin phe33cys variant. *Protein Science*, 2003.

[54] Matthew Z Tien, Austin G Meyer, Dariya K Sydykova, Stephanie J Spielman, and Claus O Wilke. Maximum allowed solvent accessibilities of residues in proteins. *PLoS ONE*, 8(11):e80635, 2013.